minerals

MDPI

Article

Geochemistry and Petrogenesis of the Ediacaran Post-Collisional Granitoid Rocks in the Midyan Terrain, Northern Arabian Shield, Saudi Arabia

Aref Lashin [1,*], Mohammed Abu Anbar [2,*], Essam Aboud [3], Faisal Zaidi [4], Abdulaziz Al-Bassam [4], Nassir Al Arifi [4] and Emad Al-Homadhi [1]

[1] Petroleum and Natural Gas Engineering Department, College of Engineering, King Saud University, P.O. Box 800, Riyadh 11421, Saudi Arabia
[2] Geology Department, Faculty of Science, Tanta University, Tanta 31527, Egypt
[3] Geohazards Research Centre, King Abdulaziz University, P.O. Box 80206, Jeddah 21589, Saudi Arabia
[4] Geology and Geophysics Department, College of Science, King Saud University, P.O. Box 2455, Riyadh 11451, Saudi Arabia
* Correspondence: arlashin@ksu.edu.sa (A.L.); mmanbar@science.tanta.edu.eg (M.A.A.)

Abstract: Midyan granites are located in the northern Arabian shield, northwest Saudi Arabia, in the Midyan terrain. They represent the most northerly segment of the Arabian–Nubian shield, which comprises the northern part of the East African orogeny. Consequently, understanding the origin of post-collisional and anorogenic magmatism in the Midyan terrain has significant geodynamic implications. Midyan granites are mainly composed of alkali feldspar granite, syenogranite, and rarely of granodiorite and diorite. Most of the studied granites are alkali-calcic, calc-alkaline, and metaluminous to peraluminous magma types. They are characterized by enrichment with light rare earth elements (LREEs), large-ion lithophile elements (especially Rb and Th), and some high-field strength elements (HFSE, e.g., Nb, Ta, Zr, and U), and the slight depletion of heavy rare earth elements (HREEs). Therefore, the Midyan granites and Hael granites studied in this paper represent good sources of geothermal heat, uranium–thorium, and REE mineralization. The studied granites have moderately strong negative Eu anomalies and a distribution pattern that is very consistent with that of the upper crust, indicating the presence of plagioclase or potassium feldspar cumulates. They have a Th/Ta ratio similar to that of the source of the crust, which may be derived from the upper crust following the collision between East and West Gondwana in the final stage of the Arabian Shield evolution. The data presented in this study are therefore consistent with the post-collisional intraplate magmatism that occurred at the beginning of the transition from convergent to extensional tectonics. The studied granites are derived from melt generated at a crystallization temperature of around 750°C at a pressure of around 0.2–0.5 GPa, emplaced at relatively shallow to moderate depths of between 20 and 30 km.

Keywords: Arabian–Nubian Shield; whole-rock geochemistry; granite petrogenesis; Midyan Terrain; Saudi Arabia

Citation: Lashin, A.; Anbar, M.A.; Aboud, E.; Zaidi, F.; Al-Bassam, A.; Al Arifi, N.; Al-Homadhi, E. Geochemistry and Petrogenesis of the Ediacaran Post-Collisional Granitoid Rocks in the Midyan Terrain, Northern Arabian Shield, Saudi Arabia. *Minerals* **2023**, *13*, 379. https://doi.org/10.3390/min13030379

Academic Editor: Jaroslav Dostal

Received: 31 January 2023
Revised: 27 February 2023
Accepted: 6 March 2023
Published: 8 March 2023

1. Introduction

The Arabian–Nubian Shield (ANS) is one of the largest regions of the juvenile continental crust [1] and was mostly formed during the Neoproterozoic era, as indicated by the ages of U–Pb zircon and isotopic data on Sr, Nd, and Pb [2,3]. It is covered by Precambrian metamorphic and igneous rocks around the Red Sea in northeast (NE) Africa (Egypt, Eritrea, Ethiopia, Somalia, and Sudan) and western Arabia (Saudi Arabia and Yemen). The Arabian Shield (AS) is composed mainly of well-preserved Neoproterozoic assemblages that have been slightly metamorphosed. These assemblages were generated between 900 and 550 Ma through the successive accretion of inter-oceanic island arcs along

suture zones of serpentinized ultramafic rocks of ophiolitic affinity [4]. The crust beneath the ANS was formed because of late Tonian–Cryogenian (870–635 Ma) accretion, Ediacaran (635–580 Ma) collision, and orogenic collapse [5,6].

The five main terrains of the Arabian shield (AS) are the Midyan, Hijaz, Ar Rayn, Asir, and Afif composite terrains, which are shown in Figure 1. The terrains' evolution essentially occurred due to the formation of an island-arc crust or continental marginal-arc crust above the evolving subduction systems during the late Proterozoic [4]. The Midyan terrain is composed of deformed layered rock units intruded by diorite, tonalite, granodiorite (arc-related, 680 Ma), and younger I-type granites.

Granitoids constitute a major Arabian Shield (AS) component and were emplaced at different crustal levels with variable geochemical characteristics, tectonic settings, and ages [7,8]. The AS includes one of the largest peralkaline granite provinces in the world. At least 49 separate alkaline-to-peralkaline granite intrusions are known, with a total outcrop area exceeding 5000 km^2 constituting approximately 2.35% of the Arabian Shield [9].

The alkaline and post-collisional granites represent the youngest phases of magmatic activity in the Arabian Shield and, are of economic interest because they are commonly enriched with U, Th, Nb, Ta, Sn, W, Mo, Zr, Y, and REE. Additionally, there is a close relationship between rare metal mineralization and alkaline granites, which is demonstrated in the Midyan region. They are diverse in their geochemical characteristics, origins, and geotectonic evolution. Five felsic intrusive rocks from the Midyan terrain were studied by Bakhsh and Alderton [10].

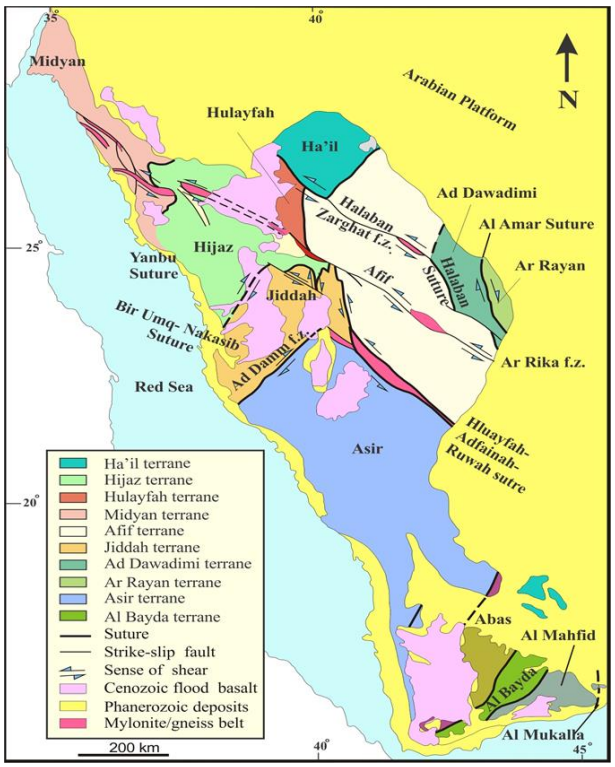

Figure 1. Tectonostratigraphic terrains in the Arabian shield, including Saudi Arabia and Yemen (modified after Stoeser and Camp [11], Windley et al. [12], and Johnson and Woldehaimanot [13]).

The granites contain relatively high REE and rare metal content. Geochemical studies have determined the economic significance of the studied granitoid and alkali granites in the Midyan terrain, as they are the most promising hosts for enrichment with REEs and rare metals. In addition, these granitoids are enriched with the radioactive elements uranium (U), thorium (Th), and potassium (K), which makes them good candidates for use in enhanced geothermal systems (EGS) for possible energy production.

This work forms part of a project that deals with the enhanced geothermal systems of high-heat-generating granite northwest of Saudi Arabia. The project area covers the whole Midyan terrain, including the NEOM area, hence the importance of this work. The NEOM area is at the core of the 2030 Saudi Vision, which aims to create a new community based on renewable and sustainable energy and to construct the largest open-air resort in the world (a cave-based resort that is mainly encased in exposed granitic rocks). The project contains a variety of geophysical, water hydrochemistry, and rock geochemical investigation techniques.

This study aims to discuss field observations, petrographical, mineralogical, and geochemical studies to interpret the origin, petrological and geochemical significance, magmatic processes, and tectonic evolution of Midyan granites. Studying the granites in the Midyan terrain is of great importance for testing concepts about continental growth in the northern ANS. Additionally, the present data, in conjunction with some published data, were used to construct a model that describes the petrogenetic evolution of the northern Arabian Shield during the late Neoproterozoic.

2. Regional Geology

The Midyan terrain crops out in the northwestern part of the Arabian Shield, as suggested by Stoeser and Camp [11], Windley et al. [12], and Johnson and Woldehaimanot [13] (Figure 1). The granitoid rocks under study occur in the Midyan terrain, which comprises approximately 60% of the Precambrian outcrop [14]. Figure 2a shows a geological map of the Proterozoic rocks in the western part of Saudi Arabia, which includes the Midyan terrain compiled by Johnson [15].

The granitoid rocks in the Midyan terrain are represented by the Al Bad super suite and Muwaylih suite (Figure 2a) and consist of about 80 plutons. The Al Bad granite super suite occurs in the northwestern part of the AS and constitutes a large group of post-tectonic granites that range in age from middle to late Ediacaran (575–570 Ma). It is composed mainly of alkali feldspar granite and syenogranite, with anomalous high radioactivity in some plutons. It is considered a good source of uranium and rare earth elements [16], as well as beryllium, fluorine, tin, and tungsten.

Another group named the Muwaylih suite crops out in the central part of the Midyan terrain in the form of plutonic rocks (Ramsay et al., 1986), and comprises mafic plutons that intrude the Zaam and Bayda groups and the Najah granodiorite in the central part of the Midyan terrain. The plutons are variably metamorphosed and deformed, and their contacts vary from discordant in some places to concordant in others. The main rock types in the suite are tonalite, trondhjemite, diorite, quartz diorite, gabbro, and norite, with ages ranging between 710 Ma and 725 Ma [17].

Both plutonic rocks in the Midyan terrain (the Al Bad granite super suite and the Muwaylih suite) intrude into layered volcano–sedimentary country rocks represented by the following rock units, as compiled by Johnson [15] (Figure 2a).

1. The Ghawjah Formation occurs on either side of Wadi Ghawjah, inland from Al Muwaylih in the Midyan terrain, as a succession of metavolcanic and metasedimentary rocks (more than 710 Ma). It is intruded by the Muwaylih suite (725–710 Ma) and is, therefore, older than 710 Ma [18].
2. The Hegaf Formation occurs in the northwestern part of the Midyan terrain (more than 710 Ma), and is conformably overlain by the Silesia Formation and unconformably overlain by the Amlas Formation [19,20].
3. The Zaytah Formation occurs in the northern part of the Midyan terrain as a succession of felsic lava and tuff, tuffite, graywacke, and mafic and felsic schists that have metamorphosed to greenschist facies [20]. This formation is broadly correlated with the Silesia and Hegaf formations, with an age of more than 710 Ma.
4. The Amlas Formation occurs as a long belt about 60 km long in the northern part of the Midyan terrain and is mainly composed of metasediments and subordinate volcanic rock that is partly bounded from the north and south by ultramafic-decorated fault zones [20].

5. The Hinshan Formation crops out east of Haql in the extreme northwestern part of the AS. It comprises intermediate to felsic volcanic and sedimentary rocks that have metamorphosed to greenschist facies and includes andesitic and rhyolitic flows, tuffs, minor basalt, and well-bedded and locally graded graywacke, siltstone, and shale [21].

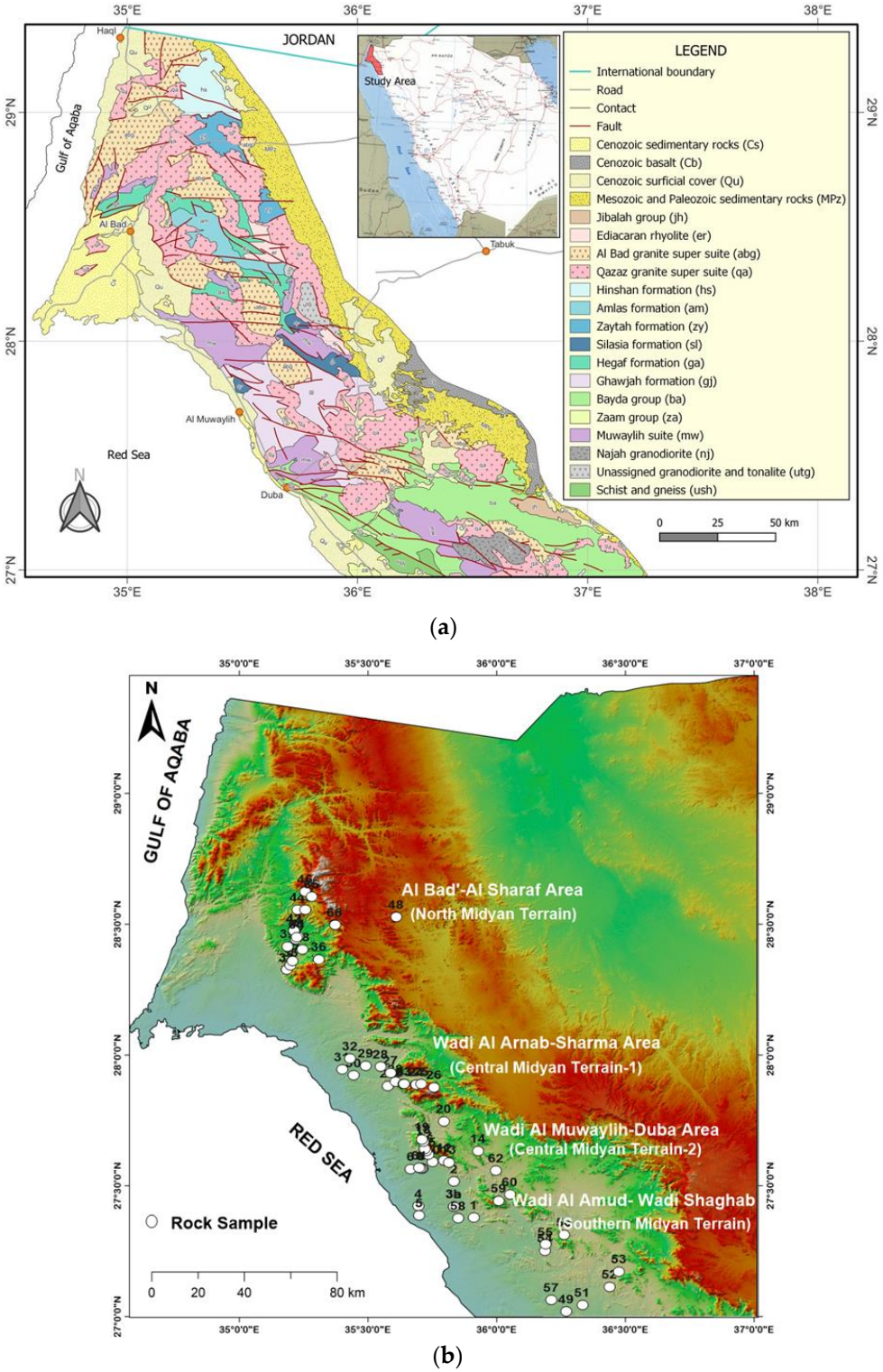

Figure 2. (**a**) Midyan terrain in a compiled geologic map of Proterozoic geology of western Saudi Arabia (modified from Johnson [15]). (**b**) Sample locations in the studied area.

3. Materials and Methods

3.1. Fieldwork

The fieldwork was carried out on different granitoid rocks in the Midyan Terrain on asphaltic roads that pass through Duba, Al Muwaylih, and Al Bad, and included field relations and observations. Approximately 200 representative samples were collected from different rock varieties in different granitic plutons in the Midyan terrain.

3.2. Petrography and Mineralogy

Approximately 100 thin sections were prepared from the representative granites and dykes to study their petrography and mineralogy. A petrographic examination of thin sections was carried out using a polarized microscope. Photomicrographs of the rocks were taken using a camera attached to the polarized microscope under cross- and plane-polarized light. The thin sections of crystals' length and width were measured manually using the scale in the microscope eyepiece. The percentage of each mineral was determined using a point counter unit attached to the polarized microscope.

3.3. Whole-Rock Geochemistry

Whole-rock chemical analyses of major, trace, and rare earth elements were performed for 49 representative fresh rock samples from the granites and dykes from the studied areas (12 from northern Midyan terrain, 6 from central Midyan terrain-1, 24 from central Midyan terrain-2, 5 from southern Midyan, and 1 from the Hael area). The major elements were determined using X-ray fluorescence spectrometry after fusing a 0.66 g sample powder using $Li_2B_4O_7/LiBO_2$ fusion. Trace elements, including REE, were determined using inductively coupled plasma mass spectrometry (ICP-MS). All analyses were performed by Bureau Veritas Commodities Ltd., Canada. The bulk rock analysis data are presented in Tables S1–S5. Geochemical data processing and plotting were carried out using Geochemical Data Toolkit software (GCDkit, [22]).

4. Results

4.1. Field Description

The studied granites are located in the northern Arabian Shield, northwest Saudi Arabia, between latitude 26°44′42.52″–28°54′42.9″ N and longitude 34°58′30.09″–36°49′39.73″ E in the Midyan terrain (Figures 1 and 2). The Midyan terrain is approximately 60 km wide from east to west and is bordered by the Gulf of Aqaba in the north, the Yanbu suture zone in the south, Phanerozoic sedimentary rocks in the east, and the Red Sea coast in the west. The studied samples in the Midyan terrain included four areas: (1) the Al Bad–Al Sharaf area (northern Midyan terrain), (2) the Wadi Al Arnab–Sharma area (central Midyan terrain-1), (3) the Wadi Al Muwalih–Duba area (central Midyan terrain-2), and (4) Wadi the Al Amud–Wadi Shoghab area (southern Midyan terrain) (Figure 2b).

In the field study in the Wadi Al Muwalih–Duba area (central Midyan terrain-2), we found high-topography alkaline granites with a white color (back), which intrude into pink granites and other phases of granite (front) (Figure 3a). These granites are buff, non-foliated, massive, without xenoliths, and coarse-grained (Figure 3b). At Wadi Muwaylih, the alkaline granites and pink granites intrude into the diorite country rocks (Figure 3c,d). The contact between them is sharp and intrusive. At the contact point with the diorite country rocks, there are some dioritic enclaves in the granites.

Figure 3. Field photographs of the studied granites showing: (**a**) alkaline granites intruding into pink granites at Wadi Muwaylih in central Midyan terrain-2; (**b**) coarse-grained pink granites at Wadi Muwaylih; (**c**) alkaline granites intruding into pink granites, and both of these intruding into diorite country rocks; (**d**) pink granites (front) intruding into diorite (background); (**e**) acidic dyke intruding into the diorite; and (**f**) sheared microgranite dyke (aplite).

The diorite country rocks are extruded by numerous acidic dykes and siliceous veins trending from NE to SW (Figure 3e). The granitic plutons in some parts of Wadi Muwaylih have been cut by faults in NW-SE and NE-SW directions, which is associated with shearing in the microgranite (aplite) dykes (Figure 3f). The outcrop at Wadi Muwaylih is a topographically high, elongated pluton; it displays several joint systems trending from NE to SW and intrudes into country rocks, mainly metavolcanics (Figure 4a), which form high-relief outcrops. Metavolcanics comprises meta-basalt and minor meta-andesites intercalated with volcaniclastic metasediments.

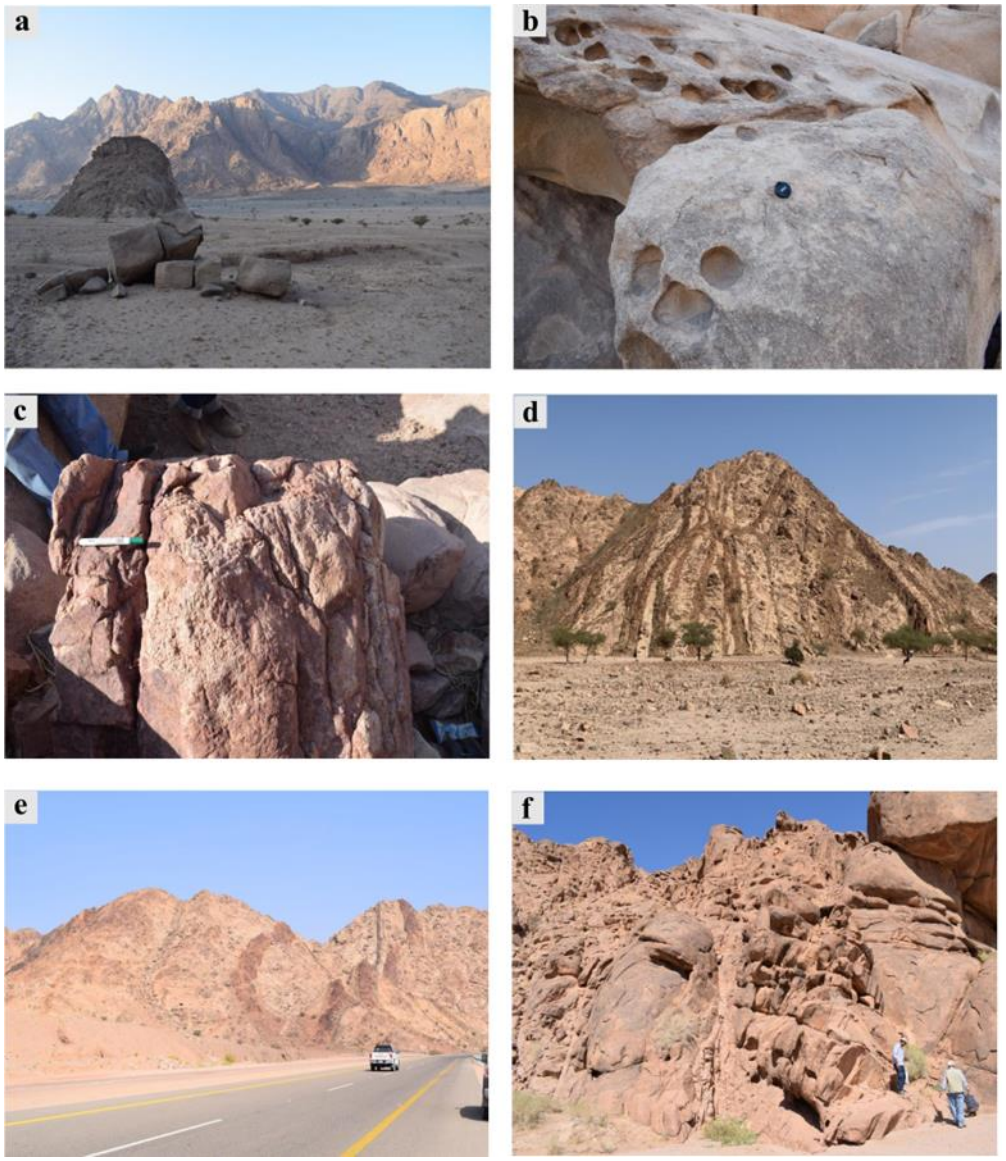

Figure 4. Field photographs of the studied granites. (**a**) Pink granites (front) intruding into metavolcanic country rocks (back) at Wadi Muwaylih; (**b**) cavernous structure in Midyan granites (central terrain-1); (**c**) pegmatite vein cutting the Midyan granites (central Midyan terrain-1); (**d**) two sets of basic dykes in two directions cutting the granite in the Midyan terrain (central Midyan terrain-1); (**e**) acidic and basaltic dykes invading the Midyan granite and displaced by a set of normal faults; (**f**) two phases of pink granite in Al-Bad, and monzogranites and alkali feldspar granites with different joint systems.

The Midyan granites in the Wadi Al Arnab–Sharma area (central Midyan terrain-1) are characterized by moderate to high topographical relief, a white color, weathering, and cavernous structures (Figure 4b). The granites in central Midyan terrain-1 are characterized by the presence of coarse-grained pegmatite veins, as shown in Figure 4c. Granites could be cross-cut by different sets of basaltic and acidic dykes trending from NW to SE and NE to SW (Figure 4d,e). Pink granites in Al Bad occur in two phases, each with different compositions. The oldest granite is mainly composed of syenogranites with numerous joints, which are more exfoliated and are intruded by alkali feldspar granites as the youngest phase (Figure 4f).

4.2. Petrography and Mineralogy

Based on fieldwork and petrographic features, Midyan granites are mainly classified into alkali feldspar granites, syenogranites, monzogranites, granodiorites, and diorites, and there are also some dykes with andesite, rhyolite, and trachyte compositions.

Alkali feldspar granites are composed mainly of potash feldspar (>90%) and quartz, with small amounts of plagioclase. Zircon, iron oxides, and apatite are the most common accessory minerals, while chlorite and sericite are secondary minerals. Potash feldspar forms euhedral to subhedral crystals measuring up to 1.5 mm × 3 mm and is represented by perthite and microcline. It contains irregular quartz and plagioclase inclusions and is actively replaced by plagioclase, which has a myrmekitic texture (Figure 5a). The microcline occurs as subhedral crystals with characteristic cross-hatched and spindle-shaped twinning (Figure 5b). Quartz forms anhedral to subhedral crystals measuring up to 1.5 mm × 2 mm and fills the interstices between the feldspar crystals. It contains plagioclase, apatite, and zircon inclusions. Plagioclase is commonly albite and forms tabular crystals which range in size from 0.2 × 0.5 mm to 1.3 × 1.8 mm. It is twinned according to the albite and Carlsbad laws. Zircon, iron oxides, apatite, and sphene are common accessory minerals (Figure 5c), whereas sericite is a secondary mineral that occurred after the alteration of the potash feldspar core (Figure 5b). These rocks are also characterized by a hypidiomorphic granular texture (Figure 5c).

Syenogranites are mainly composed of potash feldspar (90–65%), quartz, plagioclase, biotite, and muscovite (Figure 5d). Zircon, sphene, and magnetite are common accessory minerals, whereas chlorite is considered a secondary mineral. They are characterized by a hypidiomorphic granular texture. Potash feldspar usually occurs as a subhedral to anhedral perthite with small amounts of microcline and orthoclase. Perthite is represented by medium to coarse string (1.7 × 1.3 mm). Some K-feldspar mantle crystals close to the white rim of sodic plagioclase form a rapakivi texture (Figure 5e). Plagioclase occurs as subhedral to anhedral crystals and exhibits simple twinning. Quartz was found to occur as anhedral to subhedral crystals that fill the interstices between feldspar and larger interlocked crystals. Biotite represents an essential mafic constituent that forms small flakes. It has a brown color, is strongly pleochroic, changes from pale yellow to dark brown, and is partly altered to chlorite. Muscovite is represented by a few subhedral crystals and exhibits low relief. It is sometimes associated with biotite in a subparallel arrangement.

Monzogranites are mainly composed of potash feldspar, plagioclase, quartz, biotite, and subordinate muscovite. Zircon, sphene, and iron oxides are common accessory minerals. Sericite and chlorite are secondary minerals. Potash feldspar occurs as subhedral to anhedral, medium- to coarse-grained crystals measuring up to 0.8 × 1.1 mm, where perthite is the main constituent and few crystals of orthoclase and microcline are represented. Perthitic intergrowths usually occur in the form of relatively coarse strings that replace plagioclase feldspars. The quartz forms coarse- to medium-grained subhedral crystals (up to 1.4 mm). Some quartz crystals exhibit weak to strong undulose extinction. Plagioclase occurs as subhedral to euhedral elongated to stubby crystals (up to 0.5 × 0.8 mm). They usually exhibit albite twinning; some crystals are zoned, and some have sericitized cores (Figure 5f). Biotite forms subhedral to anhedral flakes measuring up to 0.3 × 0.4 mm with a brown color, and is pleochroic from yellowish brown to dark brown. Biotites fill the interstices between feldspars and are partially altered to chlorite. Muscovite is represented by a few subhedral crystals (up to 0.5 × 0.2 mm) enclosed in quartz and plagioclase and is sometimes associated with biotite in a subparallel arrangement. Opaque minerals appear as small, scattered grains and are mostly associated with feldspar and quartz crystals.

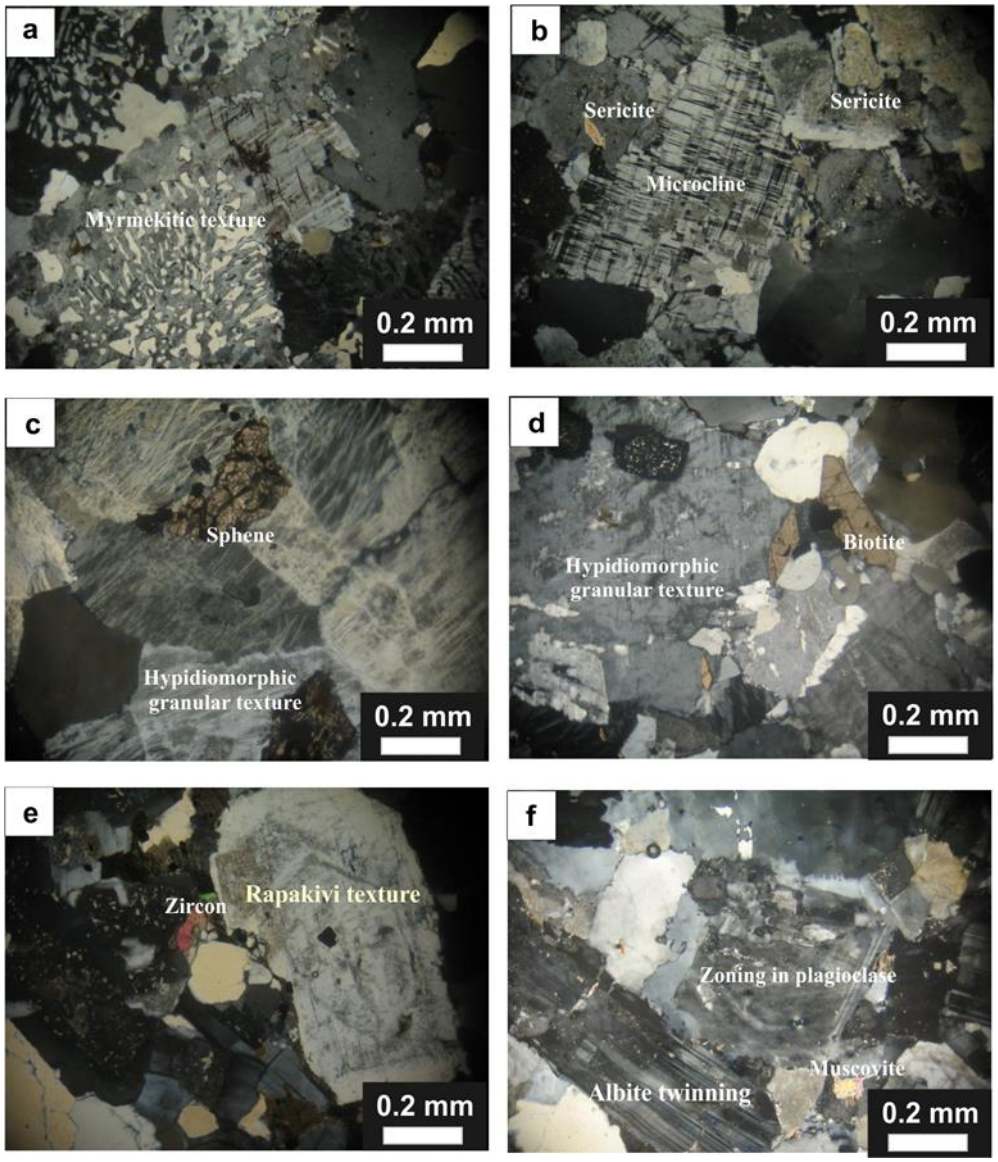

Figure 5. Cross-polarized (XPL) photomicrographs of the studied granites. (**a**) Alkali feldspar granites with myrmekitic texture; (**b**) microcline occurs as subhedral crystals with characteristic cross-hatched and spindle-shaped twinning in alkali feldspar granites; (**c**) alkali feldspar granites with hypidiomorphic granular texture; (**d**) syenogranites with hypidiomorphic texture; (**e**) rapakivi texture in syenogranites; (**f**) albite twinning in monzogranites [own source].

Granodiorites comprise plagioclase (40%–50% by volume), and quartz represents approximately 30% of the rock, whereas potash feldspar constitutes approximately 15%. The mafic minerals are hornblende and biotite. The accessory minerals are sphene, zircon, apatite, and magnetite. Chlorite and sericite are secondary minerals (Figure 6a). Plagioclase forms euhedral to subhedral elongated to stubby crystals measuring 0.6 mm to 1.1 mm. It exhibits normal zoning and albite twinning (Figure 6b). Quartz forms anhedral to subhedral coarse crystals (1.2 mm) or fills the interstices between feldspar crystals. K-feldspar occurs as subhedral to anhedral medium-grained orthoclase and perthite crystals. Biotite forms anhedral to subhedral flakes with a brown color and is strongly pleochroic from straw yellow to dark brown. Hornblende occurs as euhedral to subhedral green-colored prismatic crystals and exhibits trichroic pleochroism from greenish brown (X) to olive green (Y) to dark green (Z).

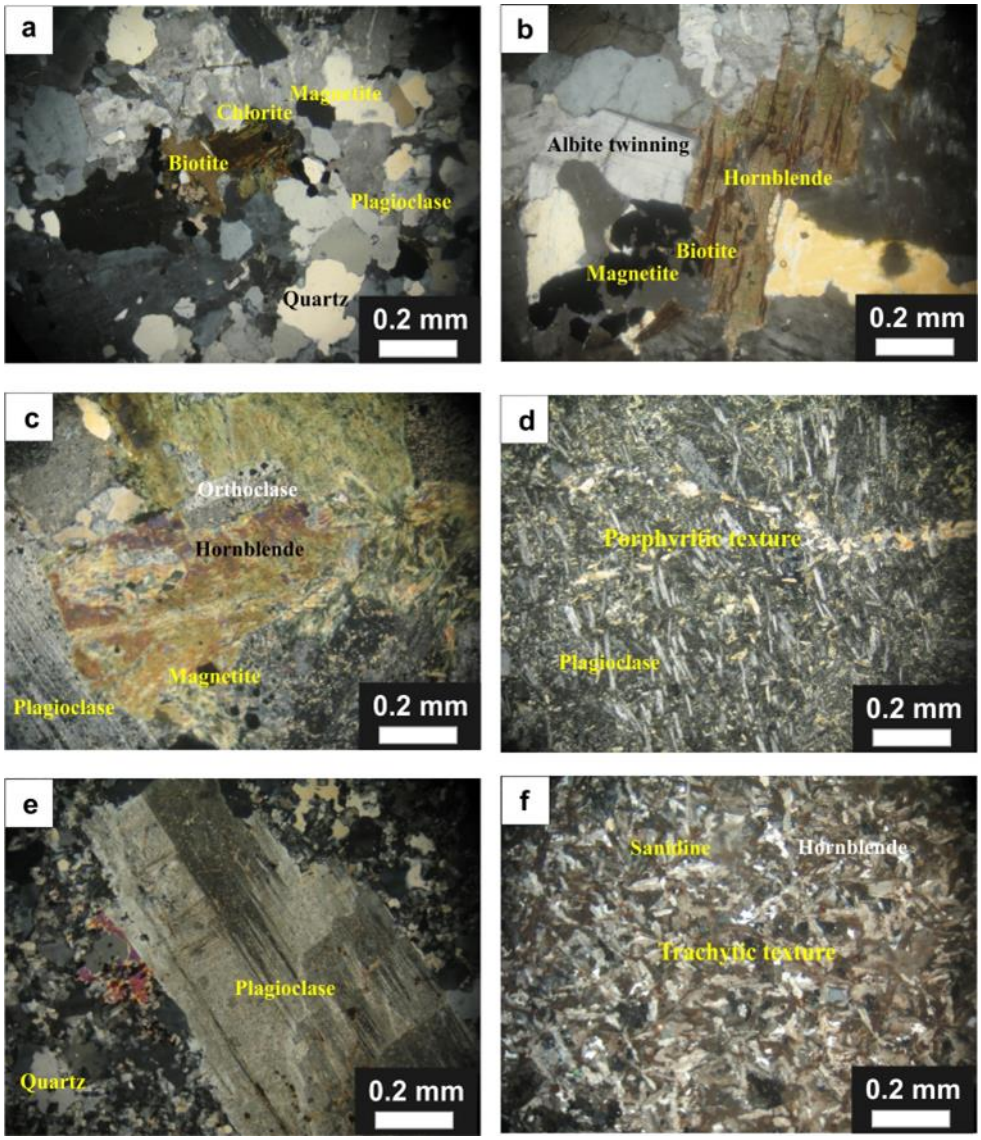

Figure 6. Cross-polarized (XPL) photomicrographs of the studied rocks: (**a**) granodiorite; (**b**) albite twinning in granodiorite; (**c**) plagioclase showing albite and Carlsbad twinning in diorite; (**d**) porphyritic texture in andesite; (**e**) rhyolite showing phenocryst of plagioclase embedded in groundmass from plagioclase and quartz; and (**f**) sanidine and hornblende in a trachytic texture [own source].

Diorites are composed mainly of plagioclase and hornblende, with minor amounts of biotite, muscovite, orthoclase, and quartz. Zircon, apatite, sphene, and magnetite are accessory minerals, whereas sericite is a secondary mineral. These rocks are characterized by an ophitic texture. Plagioclase occurs as euhedral grains of up to 4 mm in size, showing albite and Carlsbad twinning (Figure 6c). Hornblende occurs as anhedral crystals up to 5 mm in size and shows pleochroism with greenish-brown to reddish-brown to dark brown. Orthoclase occurs as rare euhedral grains up to 2 mm in size, showing Baveno twinning and minor alteration of the core. Biotite occurs as shreds up to 1 mm in size, whereas quartz grains are less than 1 mm in size and occur as anhedral crystals interstitial with the other minerals.

Silicic Dykes

Andesites are composed of plagioclase and hornblende phenocrysts, which are embedded in a fine-grained groundmass of the same composition to form a porphyritic texture (Figure 6d). Plagioclase occurs as euhedral to subhedral prismatic and tabular phenocrysts

and small laths in the groundmass. They commonly exhibit albite twinning and partial alteration. Some crystals have corroded edges owing to reactions with groundmass constituents. Hornblende is the dominant ferromagnesian mineral and commonly forms euhedral phenocrysts with perfect basal sections, which are embedded in a microcrystalline groundmass. Biotite crystals are present in small amounts, commonly disseminated in the groundmass, and sometimes altered to chlorite. Iron oxide (magnetite) occurs as anhedral fine grains in the groundmass or is associated with biotite. Quartz is less common and is found in interstitial crystals in groundmasses.

Rhyolites are mainly composed of phenocrysts of quartz, potash feldspar, and plagioclase set in a microcrystalline groundmass containing the same minerals. Iron oxides, zircons, apatite, and sphene are accessories. Chlorite is the main secondary mineral. The rock exhibits a porphyritic texture (Figure 6e), and some thin sections show spherulitic textures. Quartz occurs either as anhedral phenocrysts or as a mosaic of fine grains that form the groundmass. The quartz phenocrysts are partially replaced by ground masses. Potash feldspar is mainly represented by a microcline that forms either subhedral prismatic or rectangular phenocrysts, and fine subhedral crystals were located in the groundmass. The crystals exhibit cross-hatched twinning, which is partially sericitized. Potash feldspar is commonly associated with quartz and forms a spherulitic texture. Plagioclase occurs as a subhedral phenocryst in the groundmass; it is sometimes altered into sericite. Biotite occurs as microcrystals and yellowish-green flakes with patches and fine shreds in the groundmass. It is strongly pleochroic and is partly chloritized along its cleavage planes. Magnetite occurs as fine anhedral grains in the groundmass or is associated with biotite. The groundmass comprises very fine crystalline quartz, feldspar, and a small amount of mica.

Trachytes are composed mainly of sanidine and hornblende with a trachytic texture. The accessory minerals are iron oxides, zircon, and apatite, whereas minor amounts of kaolinite and sericite represent the secondary minerals (Figure 6f). Sanidine is the most common mineral and forms microlites with lath- or rod-like shapes. Hornblende occurs in short prismatic laths. It is green and pleochroic from greenish-brown (X) to reddish-brown (Y) to dark brown (Z). Iron oxides form in considerable amounts and occur as irregular patches and grains, which are represented mainly by magnetite and hematite. Magnetite is sometimes altered to hematite, which stains the rock with a reddish-brown color.

4.3. Whole-Rock Geochemistry

4.3.1. Major and Trace Element Characteristics

The major, trace, and rare earth elements (REE_S) of samples from the studied Midyan and Hael terrains are listed in Tables S1–S4. Most varieties have SiO_2 concentrations greater than 70% and are thus classified as highly evolved felsic rocks. On a total alkali and silica (TAS) classification diagram [23] and in an R1-R2 multicationic diagram [24], the samples are mostly plotted in the alkali feldspar granite and syenogranite fields. Few samples (sample nos. 1, 3A, 5, and 52) are scattered within the fields of gabbro, granodiorite, syenite, and diorite, respectively (Figure 7a,b); this is consistent with the silica identification results.

The classification scheme of Frost et al. [25] is based on three variables: the Fe* index, the modified alkali–lime index (MALI), and the aluminum saturation index (ASI). With respect to the Fe* index, defined as FeO(t)/(FeO + MgO), most samples belong to the ferroan series, except for some samples plotted in the magnesian field near the critical line (Fe* = 0.64–0.99) (Figure 7c). According to the MALI ($Na_2O + K_2O - CaO$) (Figure 7d), the samples from the granitoid rocks are mainly plotted in the alkali-calcic and calc-alkaline fields. According to the ASI, defined as Al/(Ca 1.67P + Na + K), the studied granites are slightly metaluminous to peraluminous (Figure 7e).

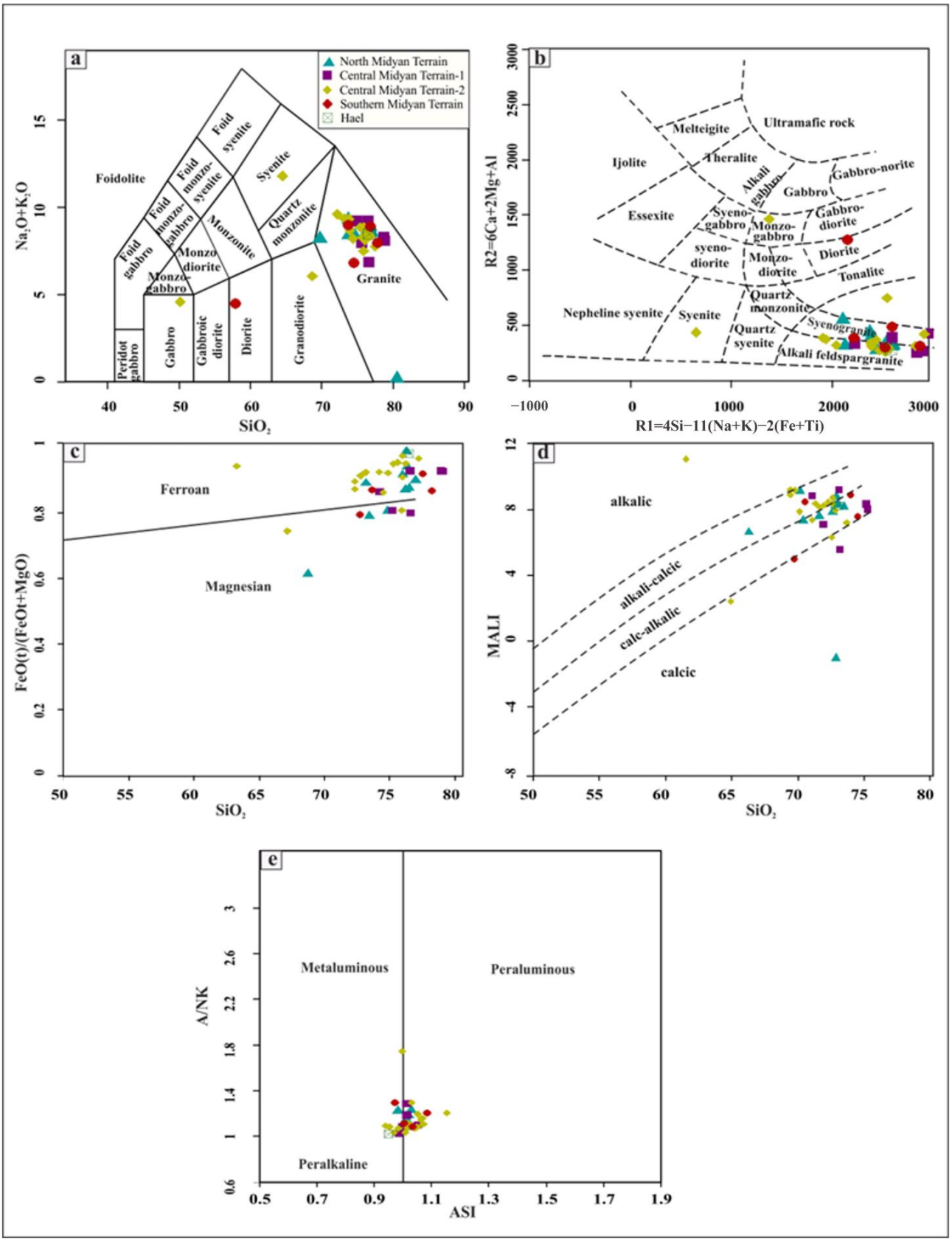

Figure 7. (**a**) SiO_2 − (Na_2O + K_2O) diagram for chemical classification of the studied granites; (**b**) geochemical classification of plutonic rocks using parameters R1 (4Si − 11(Na + K) − 2(Fe + Ti) and R2 (6Ca + 2Mg + Al); (**c**) FeO(t)/(FeOt + MgO) vs. SiO_2; (**d**) MALI vs. SiO_2; (**e**) ASI vs. A/NK.

The major elements of the studied granites form a well-defined trend on the Harker diagram plots (Figure 8a), as TiO_2, P_2O_5, CaO, Fe_2O_3, Al_2O_3, MgO display negative correlations with SiO_2, and K_2O displays a positive correlation with SiO_2. The overall pattern of decreasing TiO_2, CaO, Fe_2O_3, and MgO is characteristic of fractionating granitic systems.

4.3.2. Trace and Rare Earth Elements

Some selected trace elements show simple fractionation trends with SiO_2 (Figure 8b). Among the large-ion lithophile elements (LILEs), Cs (0.2–5.3 ppm), Rb (6.6–226 ppm), Ba (21–815 ppm), and Sr (14–228 ppm) show wide variation. Ba and Sr contents are negatively correlated with SiO_2, while Rb content is positively correlated with SiO_2. These trends indicate that the studied granites are co-magmatic, and their evolution is mainly controlled by the fractionation of quartz, feldspars, and mica. The geochemical behaviors of high-field-strength elements (HFSEs) are very similar because they are highly insoluble in aqueous fluids, and thus, tend to be very immobile.

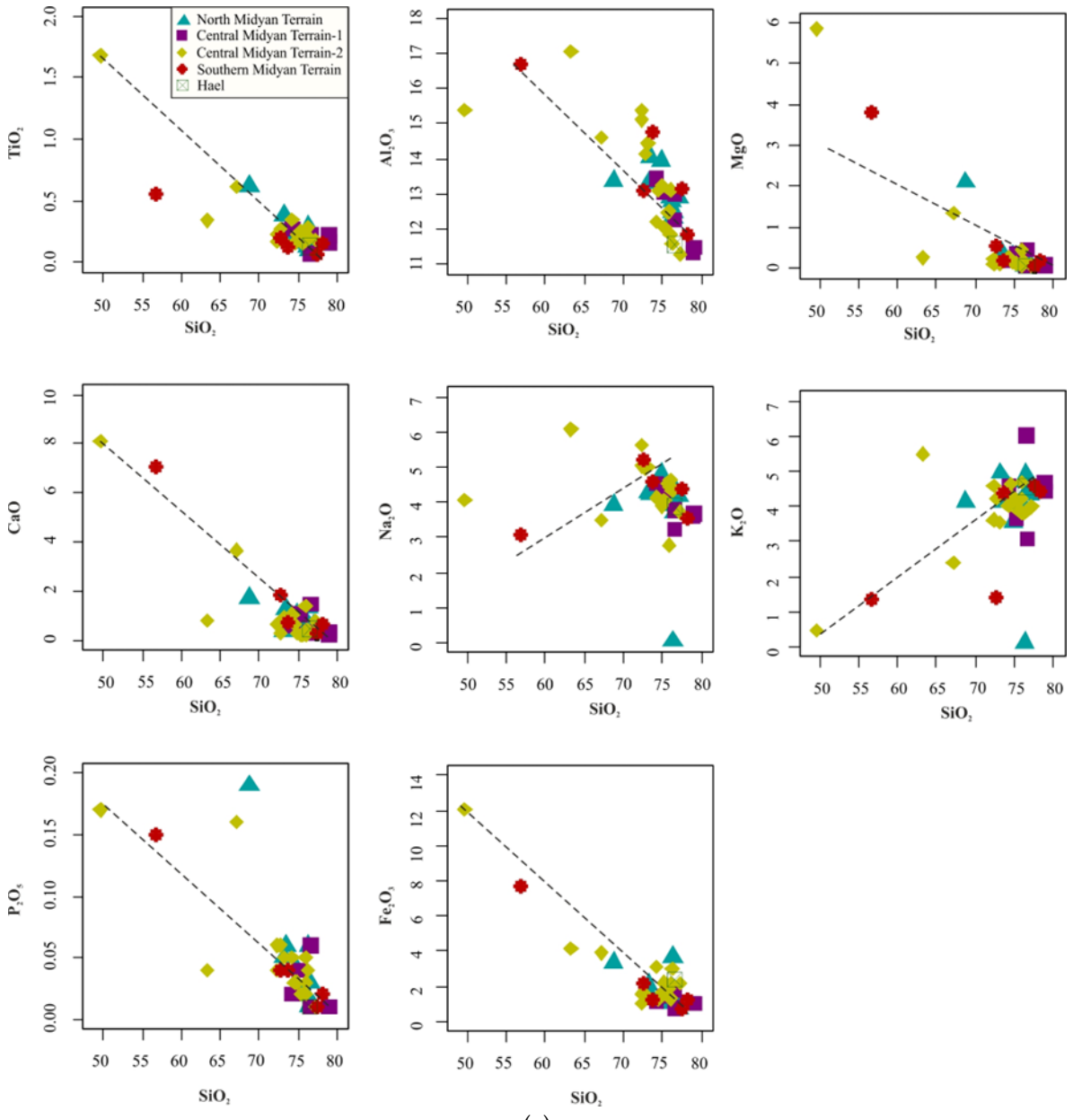

(**a**)

Figure 8. *Cont.*

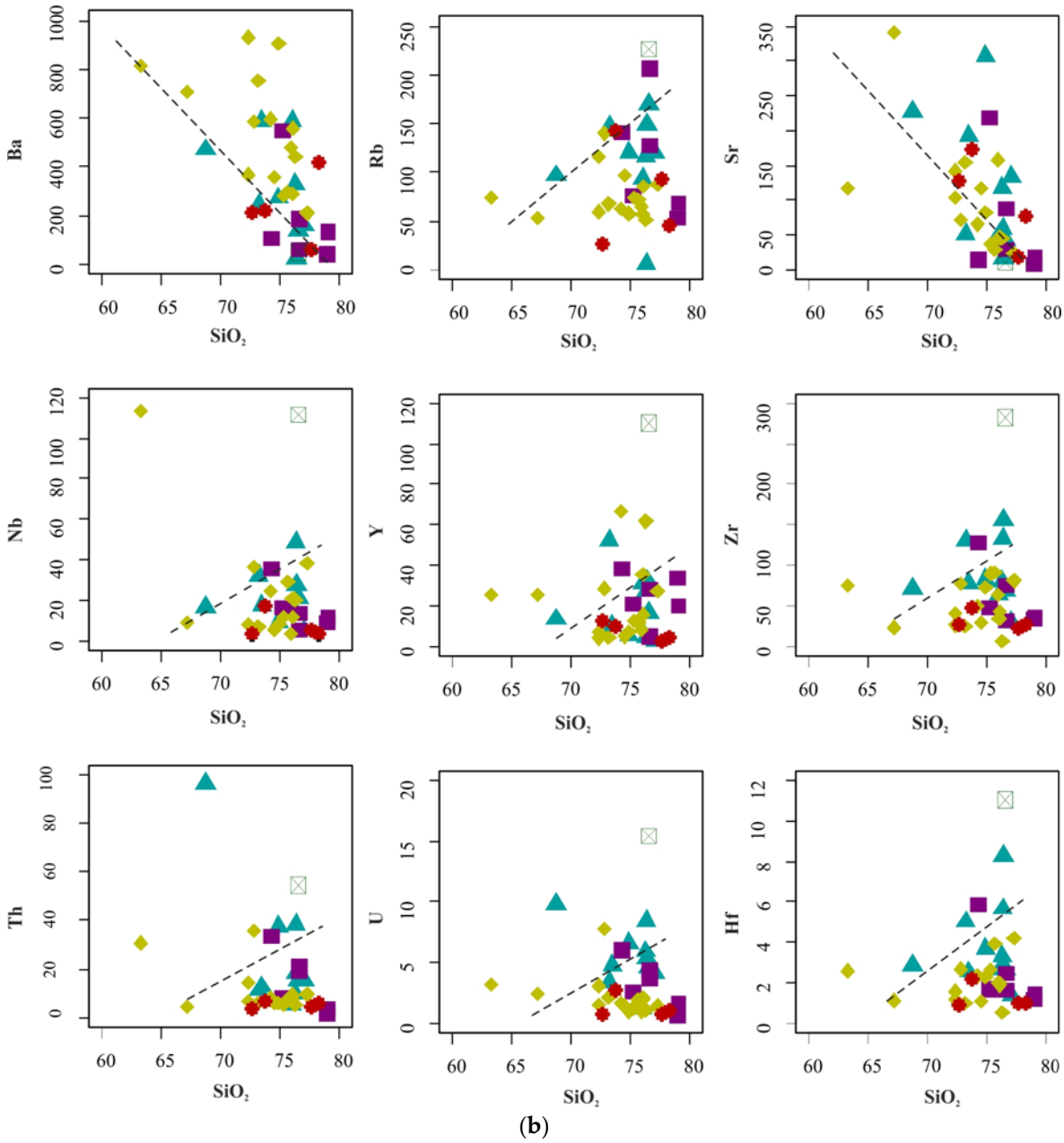

Figure 8. (**a**) Harker variation diagrams of major oxides versus SiO_2 (wt. %) for the studied granites. (**b**) Harker variation diagrams of some trace elements (ppm) versus SiO_2 (wt.%).

In the studied granites, the contents of HFSEs, such as Y (2.6–110 ppm), Zr (6.9–282 ppm), Hf (0.93–5.83 ppm), Nb (3.6–48.43 ppm), Ta (0.2–7.7 ppm), Th (1.35–54.4 ppm), and U (0.7–98 ppm), vary considerably. Zr, Nb, Th, U, and Hf concentrations are positively correlated with SiO_2 (Figure 8b).

The present data were normalized to the primitive mantle [26] (Figure 9a). It is evident from the figures that granites from different locations are characterized by high concentrations of some large-ion lithophile elements (especially Rb, Th, U, and Pb) and some high-field-strength elements (HFSE, e.g., Nb, Ta, Zr, and U); these are important sources of geothermal heat for the studied granites. In contrast, low concentrations of Cr, Ni, Sr, Ti, and Ba were observed. These geochemical characteristics are similar to those of crust or arc magmatic rocks [27].

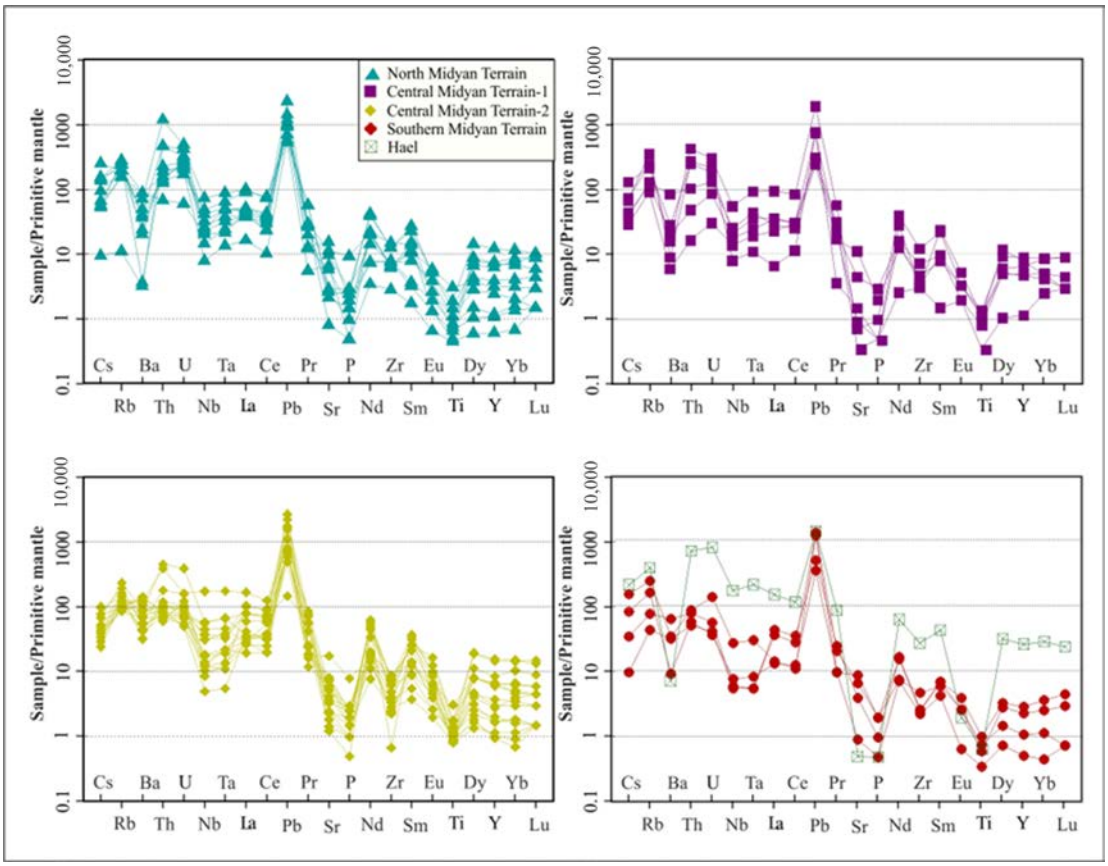

(**a**)

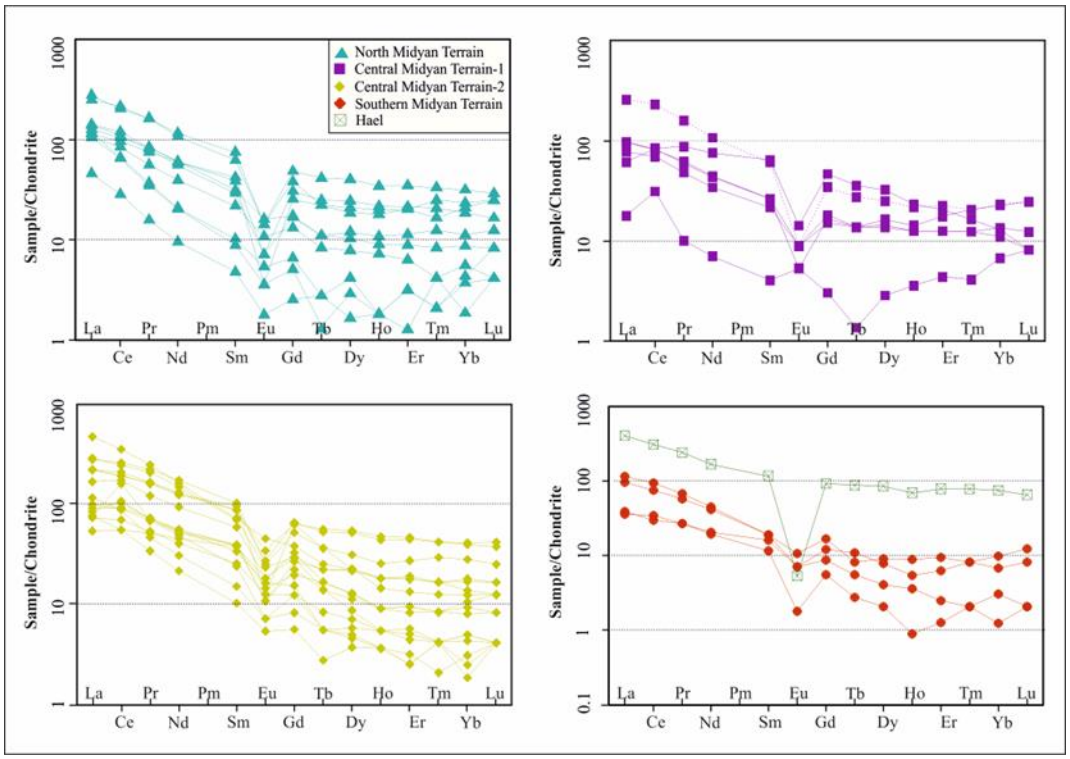

(**b**)

Figure 9. (**a**) Primitive mantle-normalized trace element patterns of the studied granites. (**b**) Plots of chondrite-normalized REE content of the studied granites.

The chondrite-normalized REE patterns [28] (Figure 9b) of the studied granites indicate that these rocks have similar geochemical characteristics. They are characterized by considerably greater variation in total rare earth element (∑RRE) content (36.25–474.59 ppm), enrichment with LREEs (La/Sm) (CI = 0.95–11.91), and the slight depletion of heavy REEs (HREEs) (Gd/Lu) (CI = 0.37–6.91). All samples have moderately strong negative Eu anomalies (Eu/Eu* = 0.11–1.52) and a very consistent distribution pattern with the upper crust, indicating the presence of plagioclase or potassium feldspar cumulates [29].

4.3.3. Whole-Rock Geochemistry of Silicic Dykes

The whole-rock geochemical data of nine volcanic samples (seven from central Midyan-2 and two from northern Midyan) are listed in Table S5. The classification diagram of SiO_2 versus (Zr/Ti) (Figure 10a), from Winchester and Floyd [30], showed different compositions, i.e., three rhyolite (sample nos. 11, 13B, and 66), three trachytes (sample nos. 3B, 9, and 61), one basalt (sample no. 6), one rhyodacite (sample no. 43), and one andesite (sample no. 4).

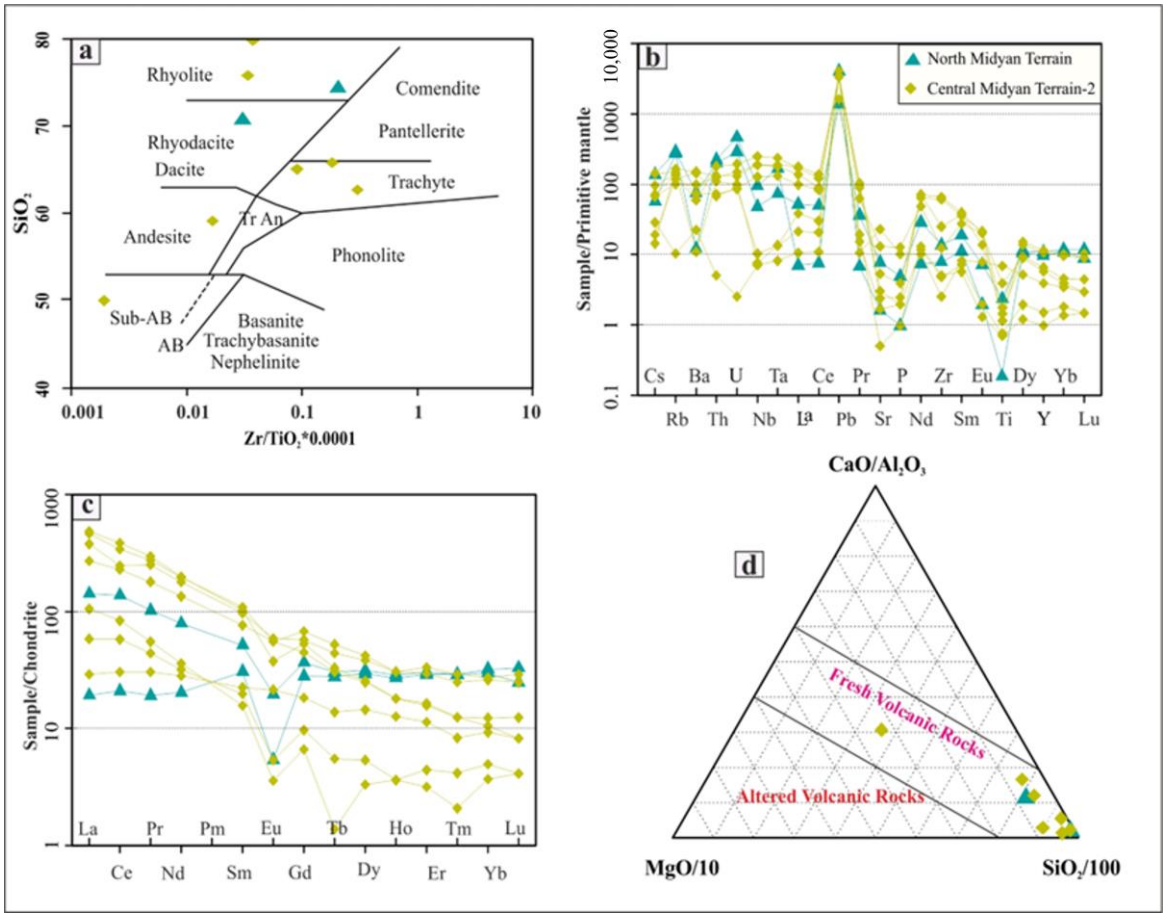

Figure 10. (**a**) Diagram of Zr/Ti versus SiO_2; (**b**) spider diagram of primitive mantle-normalized trace elements; (**c**) plots of chondrite-normalized REE content from the studied dykes; (**d**) ternary diagram of CaO/Al_2O_3–$MgO/10$-$SiO_2/100$.

The present data were normalized to the primitive mantle [26]. It is evident from the figure that the dykes show similarities in Cr, Ba, Ni, and Sr depletion, and in Rb, Nb, Zr, U, Pb, and Y enrichment (Figure 10b). The chondrite-normalized REE patterns [28] of the studied dyke samples indicate that these rocks are characterized by enrichment with LREEs and slight HREE depletion (Figure 10c). Moreover, they are characterized by medium to high total rare Earth element (∑RRE) content (58.59- 504.48 ppm).

Schweitzer and Kröner [31] used a CaO/Al_2O_3- $MgO/10$- $SiO_2/100$ ternary diagram to demonstrate the alteration and mobility of elements in the studied dykes. The analyzed samples are plotted inside the field of fresh volcanic rocks (Figure 10d).

Al Malabeh [32] (1993) distinguished between rift volcanics of crustal fragmentation and plateau volcanics of true continental origin using the $K_2O/(Na_2O + K_2O)$ versus TiO_2/P_2O_5 diagram proposed by Chandrasekharam and Parthasarathy [33]. The rocks under consideration were plateau volcanics of true continental origin (Figure 11a). The parental Magma of the studied volcanic rocks had SiO_2 and K_2O content that was consistent with alkaline to sub-alkaline affinity, as shown in Irvine and Baragar's total alkalis versus SiO_2 diagram (Figure 11b) [34].

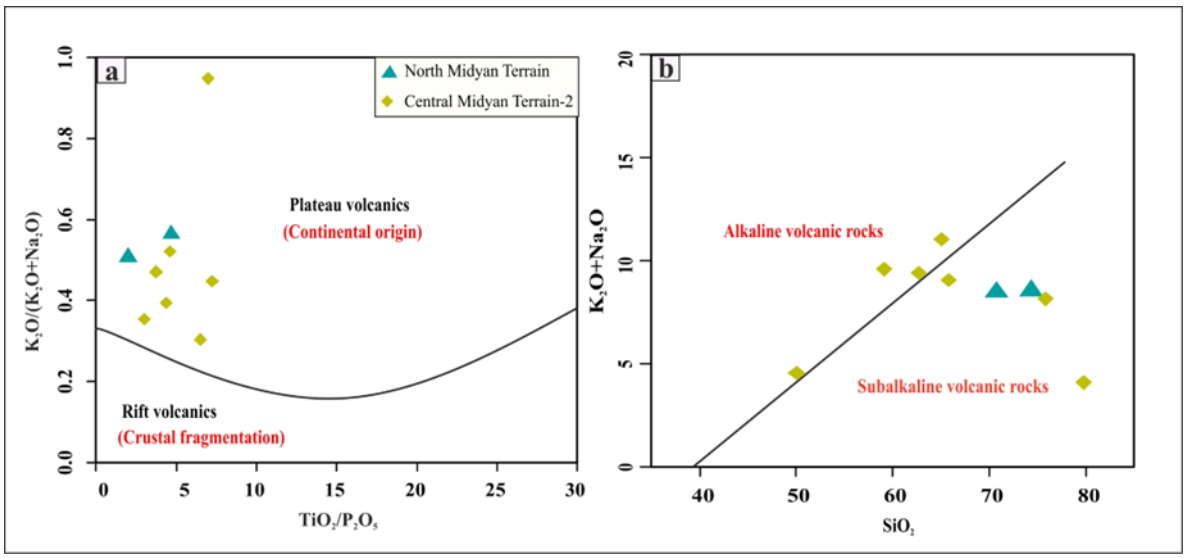

Figure 11. (**a**) Diagrams of variation in $K_2O/(Na_2O + K_2O)$ versus TiO_2/P_2O_5, and (**b**) total alkali-silica.

5. Discussion

5.1. Petrogenesis and Magma Source of Midyan and Hael Granitoids

Implications of Trace and Rare Earth Elements

Several models have been proposed to explain the origin of granitoids: (1) fractional crystallization from mantle-derived magma [35], (2) magmatic migmatization [36], (3) the partial melting of crustal rocks [37,38], and (4) a deep crustal hot zone origin [39,40].

The granitic intrusions in the Midyan and Hael areas showed more LREE enrichment compared to HREEs; were enriched with LILEs and HFSEs and relatively depleted in Sr, Nb, and P; and had negative Eu anomalies. The ratio of HFSEs in magmatic rocks can accurately reflect the characteristics of their magmatic source. The test results revealed that the average value of Rb/Nb was 8.46, which is higher than the average value of Earth's crust (4.5) [41]. The average value of Nb/Ta was 14.3, which is lower than the average value of 17.5 for the original crust but may be similar to the Nb/Ta value of crustal magma (11–12) [41]. Ba/Th was 3.08–150.85, with an average value of 45.58, which is far below the average value of the continental crust (124) [42,43]. The average value of Th/Ta was 14.1, which is much higher than that of the genetic rocks of the original mantle, and is relatively close to the mean value of the crust (Th/Ta = 11.67, [44]). The average value of Th/Ce was 0.27, which is higher than the values for mid-ocean ridge basalt (MORB, 0.016) and ocean island basalt (OIB, 0.05). This result means that subducted sediment contributed some constituents to the source [45]. In the $(La/Yb)_N - (Eu/Eu^*)$ diagram [46] (Figure 12a), most samples were plotted within the crust source, and a few samples were scattered toward the crust–mantle source. The low MgO and Cr content in the samples also indicated that the granite of the region had been partially melted from the material of the crust source material.

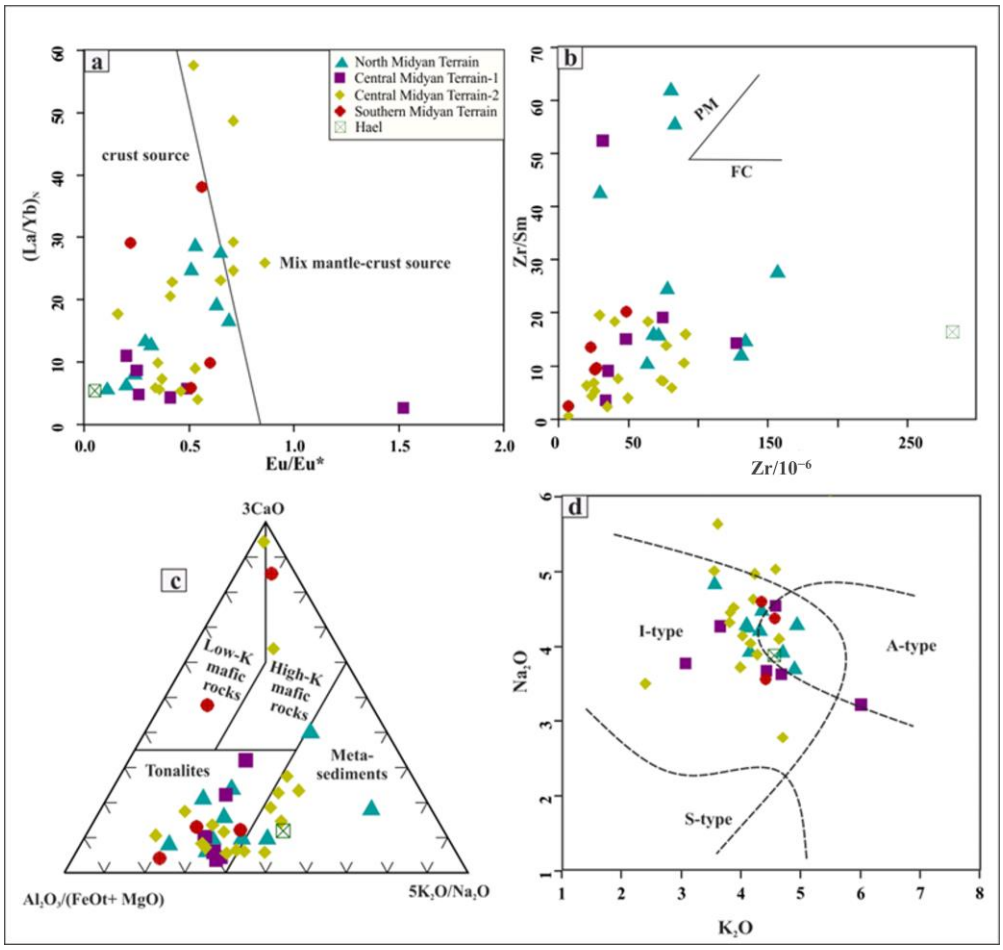

Figure 12. (**a**) $(La/Yb)_N$ − (Eu/Eu*) diagram; (**b**) Zr versus Zr/Sm diagram; (**c**) $Al_2O_3/(FeOt + MgO)$ − 3CaO − $5(K_2O/Na_2O)$ ternary diagram; (**d**) Na_2O wt% vs. K_2O wt% diagram.

The Zr versus Zr/Sm diagram [47] (Figure 12b) can be used to judge magmatic genesis, and the samples represented on the plot show a positive correlation, indicating that partial melting is the main process involved in Midyan granitoid generation.

Partial melting of the continental crust with different components produces different types of granite magma under a wide range of temperature and pressure conditions [48]. The partial fusion of sedimentary rocks in the crust usually produces acidic granites, while the partial fusion of middle and basic rocks in the crust produces I-type granite with basal alumina [49]. In the present study, the Nb/Th ratio (0.17–6.87) was similar to the ratio of the source of the crust, and significantly lower than the proportion of the mantle source (>15), suggesting that granite magma does not originate from partially melted mantle peridotite or partially melted basalt. In the $Al_2O_3/(FeOt + MgO) – 3CaO – 5(K_2O/Na_2O)$ ternary diagram (Figure 12c) proposed by Laurent et al. [50], the composition of melts derived from a potential source is determined. Most granitic samples are plotted in the field representing the melting of tonalites, and few samples occur in the field representing the melting of meta-sediments.

5.2. Typology and Tectonic Setting

Granitic rocks can be categorized into the following four main genetic types: M-type, I-type, S-type, and A-type [51,52], and can be distinguished using White and Chappell's [53] Na_2O wt% vs. K_2O wt% diagram. The studied granites were a combination of I- and A-types, except for one, which was categorized as an S-type (Figure 12d). These results were confirmed using the Zr versus SiO_2 binary diagram of Kleemann and Twist [54] (Figure 13a). Moreover, I-type granites are formed via the partial melting of intermediate-

basic igneous rocks of the crust [55]. Two chemical groups can be distinguished among the A-type granitoids. The A1 group represents distinct types of magma that settled in continental rifts or during intraplate magmatism and are derived from sources such as oceanic island basalts. The A2 group is composed of magmas derived from an underplated or continental crust that has undergone a cycle of island-arc magmatism or continent–continent collision [56]. The defined A-type varieties of the investigated areas were mostly the A1-subtype, with few samples of the A2-subtype (Figure 13b).

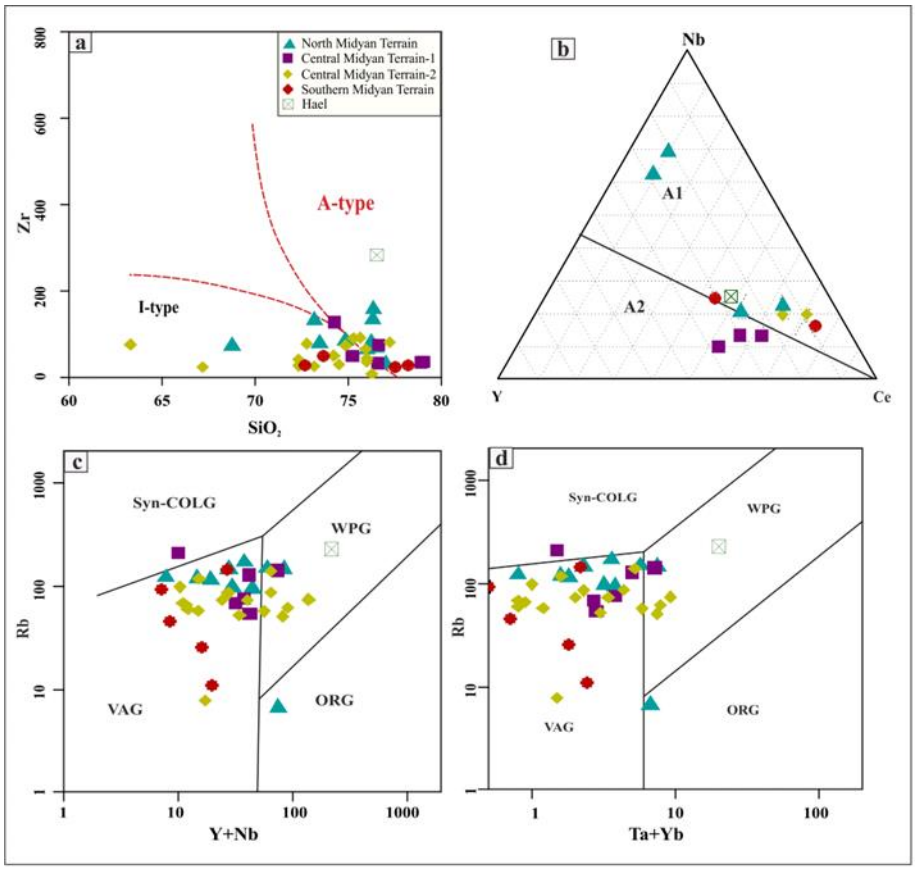

Figure 13. (**a**) Zr versus SiO_2 binary diagram; (**b**) Nb-Y-Cs ternary diagram; (**c**,**d**) Y + Nb versus Rb and Ta + Yb versus Rb discrimination diagrams.

We used a variety of tectonic discrimination diagrams [57] to constrain the tectonic environment of the granitic rocks in the Midyan and Hael areas. Samples were plotted in the fields of volcanic-arc granites (I-type) and within-plate (A-type) granites (Figure 13c,d) in Y + Nb versus Rb and Ta + Yb versus Rb discrimination diagrams. According to the Al_2O_3 versus SiO_2 diagram [58] (Figure 14a), the studied granite samples were plotted within the post-orogenic granitoid field (POG), except sample nos. 13 A and 18, which were plotted in the fields IAG + CAG + CCG. A major element system for the tectonic classification of granites was created by Batchelor and Bowden [59] (Figure 14b). The plots reveal that most granites occur in a syn-collision to post-orogenic (fields 6 and 7) tectonic setting.

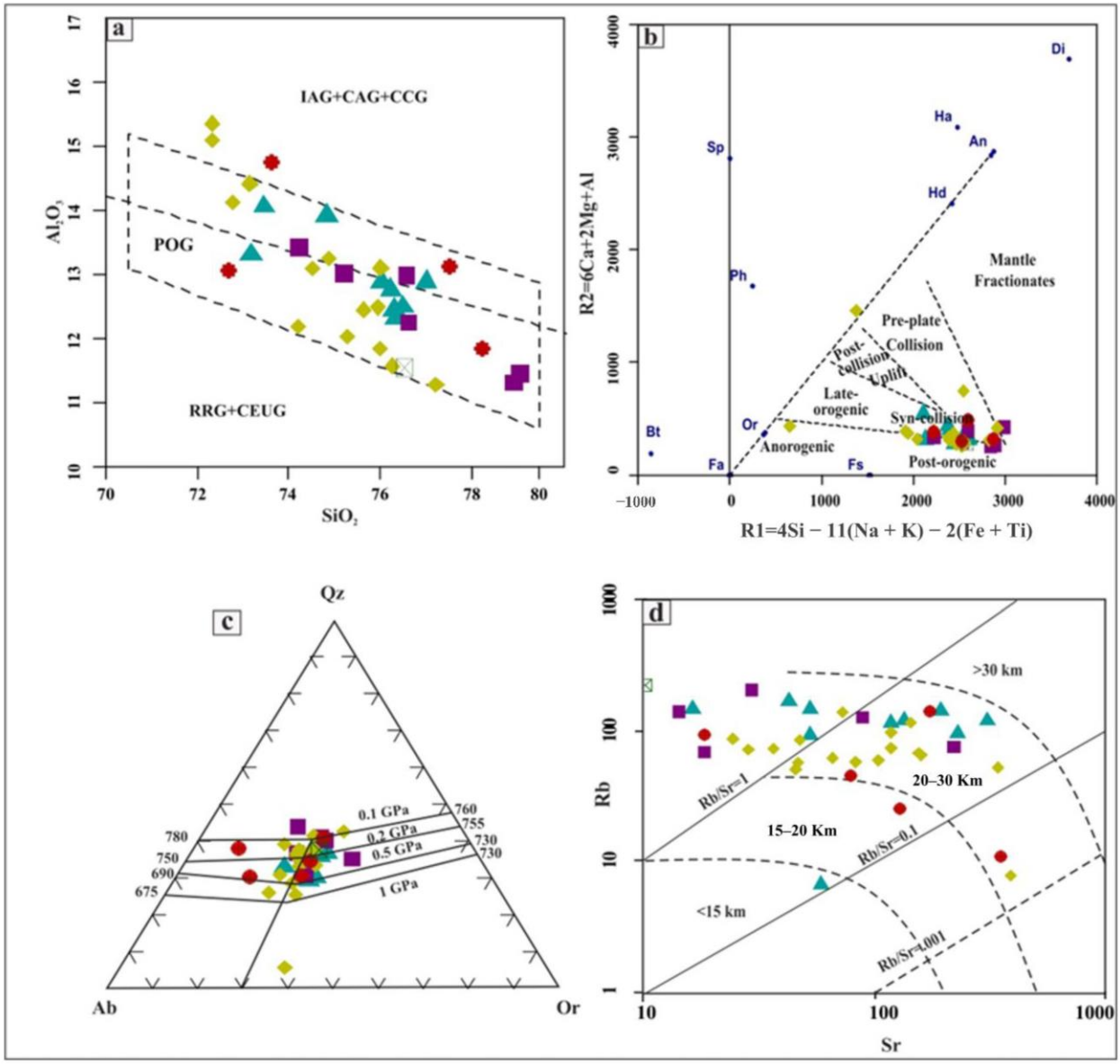

Figure 14. (**a**) Al_2O_3 versus SiO_2 diagram; (**b**) R1−R2 diagram for the studied granites; (**c**) normative Ab-Or-Qz diagram; (**d**) Rb-Sr diagram illustrating the crustal thickness during emplacement. IAG: island-arc granitoid rocks, CAG: continental-arc granitoid rocks, CCG: continental collision granitoids, POG: post-orogenic granitoids, RRG: rift-related granitoid rocks, CEUG: continental epeirogenic uplift granitoids rocks, OPG: oceanic plagiogranites, ORG: oceanic ridge granites, VAG: volcanic-arc granites, WPG: within-plate granites, and COLG: collision granites.

5.3. Estimated Temperature and Pressure of Magma

The ideal pressure and temperature conditions for the generation of granitic melts can be successfully established using the CIPW normative compositions of acidic rocks. In the normative Ab–Or–Qz diagram, the studied samples were shown to derive from a melt generated at a crystallization temperature of around 750 °C at a pressure of around 0.2–0.5 GPa (Figure 14c, from Johannes and Holtz [60]). This temperature may be similar to that estimated based on Al/Ti systematics (c. 808 °C; calculated using Jung and Pfänder's linear regression equation for igneous rock melting [61]) but was higher than the calculated Zr saturation temperature (TZr) [62,63] of 694 °C.

Miller et al. [64] showed that the average TZr for inheritance-rich granitoids is 766 °C, and for inheritance-poor granitoids, is 837°C. Consequently, we found that the rocks in the study area are inheritance-rich granitoids, i.e., saturated with zircon at the source, with

TZr < 800 °C; additionally, the TZr suggests a minimum initial magma temperature at the source.

The depletion of Sr and prominent negative Eu anomalies require the melting of a source rock within the stability field of plagioclase, which is possible in a relatively shallow domain in the crust (<30 km). The Rb-Sr diagram of Condie and Hunter [65] indicates that the studied granitic rocks are emplaced at relatively shallow to moderate depths of between 20 and 30 km (Figure 14d).

5.4. A-type Granites: Reduced or Oxidized Nature?

Contrasted FeO (t)/[FeO(t) + MgO] (F/FM) values are the most effective way to distinguish between reduced and oxidized felsic rocks [25]. We used Dall'Agnol and Oliveira's [66] F/FM versus Al_2O_3 diagram (Figure 15), which confirmed that A-type granites crystallized under reduced conditions.

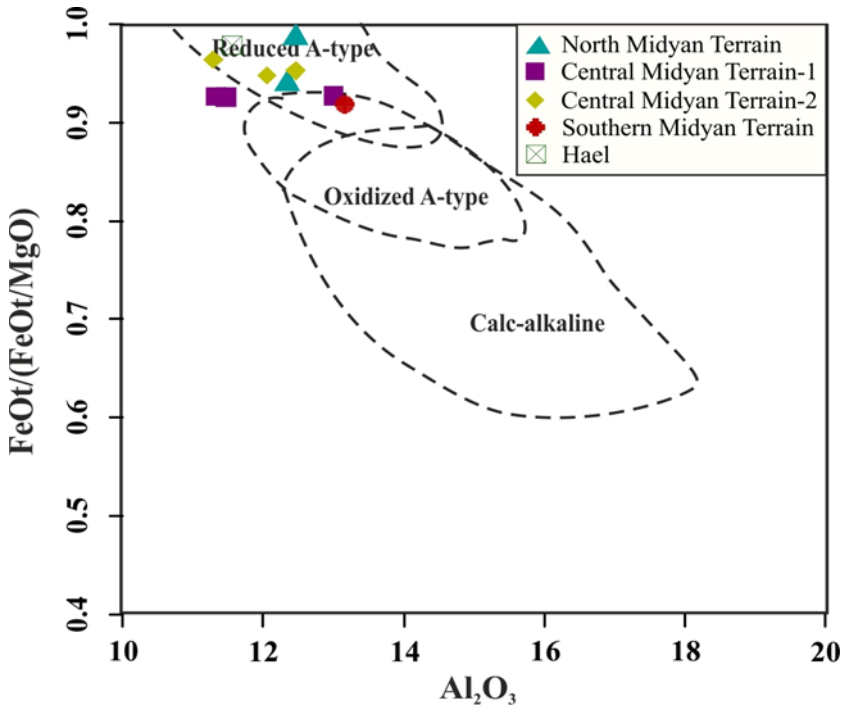

Figure 15. FeO(t)/(FeO(t) + MgO) versus Al_2O_3 (fields from Dall'Agnol and Oliveira [66]).

5.5. Tectonic Evolution

The Midyan terrain represents the most northerly segment of the ANS, which comprises the northern part of the East African orogen. Robinson et al. [67] defined the following four separate magmatic events in the ANS using U-Pb zircon dating: island-arc (~845 Ma), syn-collisional (~710 Ma), post-collisional (~620 Ma), and anorogenic (~525 Ma). Post-collisional magmatism occupies ~70% of the exposed basement outcrops in the extreme northern part of the ANS. Consequently, understanding the origin of post-collisional and anorogenic magmatism has significant geodynamic implications.

The following section presents an outline of the petrogenetic evolution of Midyan granites based on the data presented, as supported by previous data. The following four main stages are postulated (Figure 16).

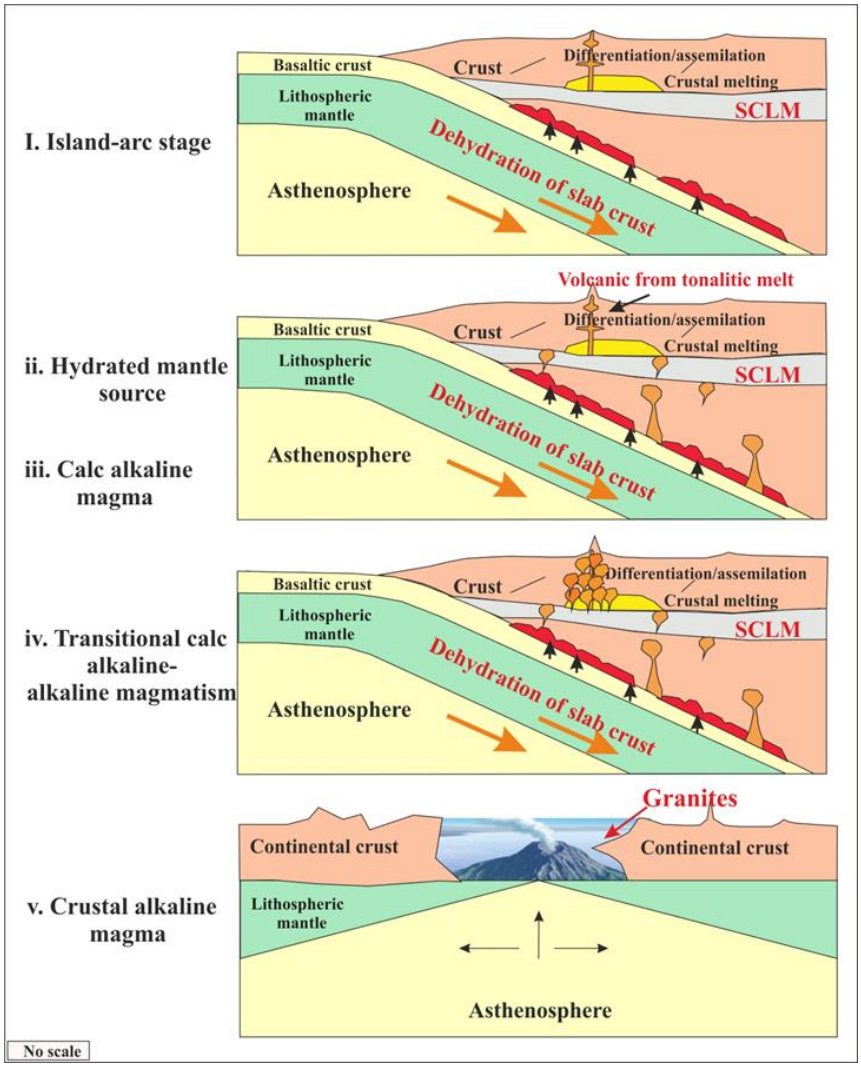

Figure 16. A proposed schematic diagram for the tectonic evolution of plutonic–volcanic rocks in the studied area.

1. The primary collisional stage, which occurred 850–620 Ma, started during the main stage of subduction with the closing of the Mozambique ocean and the initiation of the Gondwana assembly. It occurred due to dehydration of the subducted oceanic plate under relatively deep conditions (5.8–15.5 km) and favored melting of the upper mantle, which penetrated the continental crust and gave rise to calc-alkaline volcanic-arc magmatism. The arcs collided to form larger composite terrains, which are now delineated by ophiolite-decorated sutures [68]. Orogenic collapse and accretion occurred because of the closing of the Mozambique Ocean, which led to the complete cratonization and amalgamation of many distinct ANS terrains at the end of the Ediacaran period, as suggested by Johnson et al. [69].
2. Hydration of the upper mantle at 620 Ma occurred due to the melting of the oceanic subduction slab. The lower crust was then able to melt at relatively shallower depths, giving rise to more calc-alkaline granites (tonalitic melt) derived from the partial melting.
3. The dehydration and crustal incorporation stage (620–590 Ma) occurred during the warning stage of subduction, whereby orogenic magmatic activity peaked because the water supply was terminated. Calc-alkaline magmatism that occurred during the collision was followed by the formation of alkaline magma during uplifting and transcurrent movement. This event marks the post-orogenic transition from the calc-alkaline (~630–590 Ma) to the alkaline (~610–590 Ma) stage due to the relaxation

of the anorogenic regime. A large volume of post-collisional magmatic rocks was emplaced in the ANS during the period of extensional tectonism that occurred after accretion [70]. This orogenic event was followed by continued convergence and tectonic escape between 610 and 540 Ma [71–73]. This transition during ANS crust evolution has been explained as a lithospheric delamination process [74,75].

4. The anorogenic within-plate-rifting extension stage (590–560 Ma) occurred due to the partial melting of a relatively enriched source of crustal alkaline magma in the tension and relaxation stages, which raised the viscosity/lowered the pressure differentiation. Overheating and pressure accelerated the extensional regime. Thickening of the upper crust (1.2–1.5 kbar) became the predominant event. The presence of dykes in the studied areas indicates an abundance of the inferred extensional structure during this stage of ANS evolution. This was the final stage of the Neoproterozoic crustal evolution of the ANS.

6. Summary

1. Petrographically, Midyan granites are mainly composed of alkali feldspar granites, syenogranites, and monzogranites, and rarely, granodiorite and diorite. Trace element concentrations vary widely among the studied granites of the Midyan Terrain. LILEs show wide Ba variation in different areas, with an average range of 141.7 to 530 ppm; Rb content ranges between 52.65 and 186.75 ppm, whereas Sr ranges from 31.25 to 225.75 ppm. Among the HFSEs, Zr has an average range between 22.17 and 92.5 ppm, Nb has an average range between 4.02 and 26.58 ppm, Th has an average range between 4.07 and 23.12 ppm, U ranges between 0.97 and 5.08 ppm, Hf ranges between 0.93 and 4.41 ppm, and Ta ranges between 0.6 and 2.95 ppm. Hael granites show very high concentrations of trace elements, including Rb (226 ppm), Y (110.3 ppm), Zr (282.4 ppm), Th (54.4 ppm), Hf (11.01 ppm), Ta (7.7 ppm), and U (15.4 ppm). Based on the present geochemical data, the studied granites are considered good sources of REEs, radioactive elements, and geothermal heat.
2. The geochemical data of the studied granites indicate that they are mainly alkali feldspar granites and syenogranites, and rarely, granodiorite and diorite. According to their chemical characteristics, these rocks are derived from metaluminous to peraluminous magmas. The data of the studied granites were plotted in within-plate and volcanic-arc settings, which points to a post-collision origin. Midyan granites have an Nb/Th ratio similar to the average composition of the lower and upper crust, suggesting that granite magma does not originate from partially melted mantle peridotite or partially melted basalt. The studied granites are shown to derive from melt generated at a crystallization temperature of around 750 °C at a pressure of around 0.2–0.5 GPa and to be crystallized at relatively shallow to moderate depths of between 20 and 30 km
3. Whole-rock chemistry shows that the dykes extruded in the Midyan granites have rhyolite and trachyte compositions, with small amounts of basalt and andesite. The dykes are mainly composed of alkaline to sub-alkaline magma emplaced in a within-plate to volcanic-arc setting. These dykes contain plateau volcanics of continental origin. The presence of dyke swarms emplaced in the studied granites may indicate an abundance of the extensional structure during the last stage of ANS crust evolution.

Supplementary Materials: The following supporting information can be downloaded at: https://www.mdpi.com/article/10.3390/min13030379/s1, Table S1: Chemical analyses of granitic rocks of North Madyin Terrain, Table S1: Chemical analyses of granitic rocks of North Madyin Terrain, Table S2: Chemical analyses of granitic rocks of Central Madyin-1 Terrain, Table S3: Chemical analyses of granitic rocks of Central Madyin-2 Terrain, Table S4: Chemical analyses of granitic rocks of Southern Madyin Terrain and Hael and Table S5: Chemical analyses of dykes.

Author Contributions: Conceptualization, A.L., M.A.A., E.A., F.Z, A.A-B, N.A.A. and E.A.-H.; Methodology, M.A.A.; Software, M.A.A. and F.Z.; Validation, F.Z.; Formal analysis, M.A.A.; Inves-

tigation, A.L.; Resources, A.L.; Data curation, M.A.A., E.A. and F.Z.; Writing—review & editing, M.A.A.; Visualization, M.A.A. and E.A.; Supervision, A.L., E.A., A.A.-B. and N.A.A.; Project administration, A.L.; Funding acquisition, A.L. All authors have read and agreed to the published version of the manuscript.

Funding: This research was funded by the National Plan for Science, Technology and Innovation (MAARIFAH), King Abdul-Aziz City for Science and Technology, Kingdom of Saudi Arabia, Award Number (14-ENE704-02).

Data Availability Statement: Not applicable.

Acknowledgments: The authors would like also to thank the journal editor and the anonymous reviewers for their constructive reviews.

Conflicts of Interest: The authors declare that the research was conducted in the absence of any commercial or financial relationships that could be construed as a potential conflict of interest.

Abbreviations

Abbreviation	Description
ANS	Arabian-Nubian Shield
AS	Arabian Shield
XPL	Cross-polarized light
TAS	Total alkali and silica
MALI	Alkali-lime index
ASI	Aluminium saturation index
LILEs	Large-ion lithophile elements
HFSEs	High-field strength elements
CI	Chondrite
LREEs	Light-rare earth elements
TZr	Zr saturation temperature
Ab–Or–Qz	Albite- Orthoclase- Quartz
R1	$(4Si-11(Na + K) - 2(Fe + Ti)$
R2	$6Ca + 2Mg + Al$

References

1. Patchett, P.J.; Chase, C.G. Role of transform continental margins in major crustal growth episodes. *Geology* **2002**, *30*, 39–42. [CrossRef]
2. Stoeser, D.B.; Frost, C.D. Nd, Pb, Sr, and O isotopic characterization of Saudi Arabian shield 852 terranes. *Chem. Geol.* **2006**, *226*, 163–188. [CrossRef]
3. Ali, K.A.; Azer, M.K.; Gahlan, H.A.; Wilde, S.A.; Samuel, M.D.; Stern, R.J. Age constraints on the formation and emplacement of Neoproterozoic ophiolites along the Allaqi–Heiani Suture, South Eastern Desert of Egypt. *Gondwana Res.* **2010**, *18*, 583–595. [CrossRef]
4. Al-Shanti, M.A.; Pint, J.J.; Al-Juaid, A.J.; Al-Amoudi, S.A. *Preliminary Survey for Caves in the Habakah Region of the Kingdom of Saudi Arabia: Saudi Geological Survey Open-File Report SGS-OF*; Saudi Geological Survey: Jeddah, Saudi Arabia, 2003; p. 32.
5. Stern, R.J. Arc-assembly and continental collision in the Neoproterozoic African orogen: Implications for the consolidation of Gondwanaland. *Annu. Rev. Earth Planet. Sci.* **1994**, *22*, 319–351. [CrossRef]
6. Nehlig, P.; Genna, A.; Asirfane, F. A review of the Pan-African evolution of the Arabian Shield. *GeoArabia* **2002**, *7*, 103–124. [CrossRef]
7. Moghazi, A.M.; Harbi, H.M.; Ali, K.A. Geochemistry of the Late Neoproterozoic Had badh Dayheen ring complex, Central Arabian Shield: Implications for the origin rare-metal-bearing post-orogenic A-type granites. *J. Asian Earth Sci.* **2011**, *42*, 1324–1340. [CrossRef]
8. Ali, K.A.; Jeon, H.; Andresen, A.; Li, S.Q.; Harbi, H.M.; Hegner, E. U–Pb zircon geochronology and Nd–Hf–O isotopic systematics of the Neoproterozoic Hadb adh Dayheen ring complex, Central Arabian Shield, Saudi Arabia. *Lithos* **2015**, *206*, 348–360. [CrossRef]
9. Stoeser, D.B. Distribution and tectonic setting of plutonic rocks of the Arabian shield. *J. Afr. Earth Sci.* **1986**, *4*, 21–46. [CrossRef]
10. Bakhsh, R.A.; Alderton, D.H. Characterisation of granites from the Midyan terrain, NW Saudi Arabia. *Arab. J. Geosci.* **2014**, *7*, 1637–1658. [CrossRef]
11. Stoeser, D.B.; Camp, V.E. Pan-African microplate accretion of the Arabian Shield. *Geol. Soc. Am. Bull.* **1985**, *96*, 817–826. [CrossRef]

12. Windley, B.F.; Whitehouse, M.J.; Ba-Bttat, M.A.O. Early Precambrian gneiss terranes and Pan African island arcs in Yemen: Crustal accretion of the eastern Arabian Shield. *Geology* **1996**, *24*, 131–134. [CrossRef]
13. Johnson, P.R.; Woldehaimanot, B. Development of the Arabian-Nubian Shield: Perspectives on accretion and deformation in the northern East African Orogen and the assembly of Gondwana. *Geol. Soc. Lond. Spec. Publ.* **2003**, *206*, 289–325. [CrossRef]
14. Ramsay, C.R.; Drysdall, A.R.; Clark, M.D. Felsic plutonic rocks of the Midyan region, Kingdom of Saudi Arabia—I. Distribution, classification and resource potential. *J. Afr. Earth Sci.* **1986**, *4*, 63–77. [CrossRef]
15. Johnson, P.R. *Digital map of Proterozoic Rocks in Western Saudi Arabia: Meta-Data*; Saudi Geological Survey Data-File Report SGS-DF-2005-7; Saudi Arabian Directorate General of Mineral Resources: Jeddah, Saudi Arabia, 2006.
16. Drysdall, A.R. *Geology and Mineral Potential of the Granites of N.W*; Hijaz: Interim report no. 1: Saudi Arabian Directorate General of Mineral Resources Open-File Report DGMR-722; Saudi Arabian Directorate General of Mineral Resources: Jeddah, Saudi Arabia, 1980.
17. Hedge, C.E. *Precambrian Geochronology of Part of Northwestern Saudi Arabia: Saudi Arabian Deputy Ministry for Mineral Resources Open-File Report USGS-OF-04-31*; Saudi Arabian Directorate General of Mineral Resources: Jeddah, Saudi Arabia, 1984.
18. Davies, F.B.; Grainger, D.J. *Geologic Map of the Al Muwaylih Quadrangle, Sheet 27A, Kingdom of Saudi Arabia: Saudi Arabian Deputy Ministry for Mineral Resources Geoscience Map GM-82, Scale 1:250,000*; Saudi Arabian Directorate General of Mineral Resources: Jeddah, Saudi Arabia, 1985; 32p.
19. Sahl, M. *Reconnaissance Geology of the Tayyib al Ism Quadrangle, Sheet 28/34B, Kingdom of Saudi Arabia: Saudi Arabian Directorate General of Mineral Resources Open-File Report DGMR-OF-01-18*; Saudi Arabian Directorate General of Mineral Resources: Jeddah, Saudi Arabia, 1981; 24p.
20. Clark, M.D. *Geologic Map of the Al Bad Quadrangle, Sheet 28A, Kingdom of Saudi Arabia: Saudi Arabian Directorate General of Mineral Resources Geoscience Map GM-81, Scale 1:250,000*; Saudi Arabian Directorate General of Mineral Resources: Jeddah, Saudi Arabia, 1987; 46p.
21. Rowaihy, N.M. *Geologic Map of the Haql Quadrangle, Sheet 29A, Kingdom of Saudi Arabia: Saudi Arabian Directorate General of Mineral Resources Geoscience Map GM-80, Scale 1:250,000*; Saudi Arabian Directorate General of Mineral Resources: Jeddah, Saudi Arabia, 1985; 15p.
22. Janoušek, V.; Farrow, C.M.; Erban, V. Interpretation of whole-rock geochemical data in igneous geochemistry: Introducing Geochemical Data Toolkit (GCDkit). *J. Petrol.* **2006**, *47*, 1255–1259. [CrossRef]
23. Middlemost, E.A.K. *Magma and Magmatic Rocks, an Introduction to Igneous Petrology*; Longman Inc.: New York, NY, USA, 1985; 257p.
24. De la Roche, H.; Leterrier, J.; Grandclaude, P.; Marchal, M. A Classification of Volcanic and Plutonic Rocks Using R1- R2 Diagrams and Major Element Analyses—Its Relationships with Current Nomenclature. *Chem. Geol.* **1980**, *29*, 183–210. [CrossRef]
25. Frost, B.R.; Barnes, C.G.; Collins, W.J.; Arculus, R.J.; Ellis, D.J.; Frost, C.D. A geochemical classification for granitic rocks. *J. Petrol.* **2001**, *42*, 2033–2048. [CrossRef]
26. McDonough, W.F.; Sun, S.S. The composition of the Earth. *Chem. Geol.* **1995**, *120*, 223–253. [CrossRef]
27. Kelemen, S.R.; George, G.N.; Gorbaty, M.L. Direct determination and quantification of sulphur forms in heavy petroleum and coals: 1. The X-ray photoelectron spectroscopy (XPS) approach. *Fuel* **1990**, *69*, 939–944. [CrossRef]
28. Anders, E.; Grevesse, N. Abundances of the elements: Meteoritic and solar. *Geochim. Cosmochim. Acta* **1989**, *53*, 197–214. [CrossRef]
29. Li, H.; Zhou, Z.K.; Evans, N.J.; Kong, H.; Wu, Q.H.; Xi, X.S. Fluid-zircon interaction during low-temperature hydrothermal processes: Implications for the genesis of the Banxi antimony deposit, South China. *Ore Geol. Rev.* **2019**, *114*, 103137. [CrossRef]
30. Winchester, J.A.; Floyd, P.A. Geochemical discrimination of different magma series and their differentiation products using immobile elements. *Chem. Geol.* **1977**, *20*, 325–343. [CrossRef]
31. Schweitzer, J.; Kröner, A. Geochemistry and petrogenesis of early Proterozoic intracratonic volcanic rocks of the Ventersdorp Supergroup, South Africa. *Chem. Geol.* **1985**, *51*, 265–288. [CrossRef]
32. Al-Malabeh, A. The Volcanology, Mineralogy and Geochemistry of Selected Pyroclastic Cones from NE-Jordan and Their Evaluation for Possible Industrial Applications. Ph.D. Thesis, Universität Erlangen, Nurnberg, Germany, 1993; 300p.
33. Chandrasekharam, D.; Parthasarathy, A. Geochemical and tectonic studies on the coastal and inland Deccan Trap volcanics and a model for the evolution of Deccan Trap volcanism. *Neues Jahrb. Mineral. Abh.* **1978**, *132*, 214–229.
34. Irvine, T.N.; Baragar, W.R.A. A guide to the chemical classification of the common volcanic rocks. *Can. J. Earth Sci.* **1971**, *8*, 523–548. [CrossRef]
35. Chappell, B.W.; White, A.J.R. Two contrasting granite type. *Pacific Geol.* **1974**, *8*, 173–174.
36. Jahn, B.M.; Wu, F.; Chen, B. Granitoids of the Central Asian Orogenic Belt and continental growth in the Phanerozoic. *Earth Environ. Sci. Trans. R. Soc. Edinb.* **2000**, *91*, 181–193.
37. Wu, F.Y.; Jahn, B.M.; Wilde, S.; Sun, D.Y. Phanerozoic crustal growth: U–Pb and Sr–Nd isotopic evidence from the granites in northeastern China. *Tectonophysics* **2000**, *328*, 89–113. [CrossRef]
38. Koepke, J.; Feig, S.T.; Snow, J.; Freise, M. Petrogenesis of oceanic plagiogranites by partial melting of gabbros: An experimental study. *Contrib. Mineral. Petrol.* **2004**, *146*, 414–432. [CrossRef]
39. Annen, C.; Blundy, J.D.; Sparks, R.S.J. The genesis of intermediate and silicic magmas in deep crustal hot zones. *J. Petrol.* **2006**, *47*, 505–539. [CrossRef]

40. Smithies, R.H.; Howard, H.M.; Evins, P.M.; Kirkland, C.L.; Kelsey, D.E.; Hand, M.; Wingate, M.T.D.; Collins, A.S.; Belousova, E. High temperature granite magmatism, crust-mantle interaction and the Mesoproterozoic intracontinental evolution of the Musgrave Province, Central Australia. *J. Petrol.* **2011**, *52*, 931–958. [CrossRef]
41. Taylor, S.R.; McLennan, S.M. *The continental crust: Its composition and evolution*; U.S. Department of Energy Office of Scientific and Technical Information: Oak Ridge, TN, USA, 1985; pp. 301–324.
42. Saunders, A.D.; Norry, M.J.; Tarney, J. Origin of MORB and chemically-depleted mantle reservoirs: Trace element constraints. *J. Petrol.* **1988**, 415–445. [CrossRef]
43. Weaver, B.L. The origin of ocean island basalt end-member compositions: Trace element and isotopic constraints. *Earth Planet. Sci. Lett.* **1991**, *104*, 381–397. [CrossRef]
44. Rudnick, R.L.; Gao, S. Composition of the continental crust. *Treatise Geochem.* **2003**, *3*, 1–64.
45. Zhang, Y.T.; Zhang, L.C.; Ying, J.F.; Zhou, X.H.; Wang, F.; Hou, Q.L.; Liu, Q. Geochemistry and Source Characteristics of Early Cretaceous Volcanic Rocks in Tahe, North Da Hinggan Mountain. *Acta Petrol. Sin.* **2007**, *23*, 2811–2822.
46. Chen, Y.W.; Bi, X.W.; Hu, R.Z.; Qi, H.W. Comparison of geochemical characteristic of uranium- and non-uranium-bearing Indosinian granites in Guidong composite pluton. *J. Mineral Petrol.* **2009**, *3*, 106–114, (In Chinese with English Abstract).
47. Schiano, P.; Monzier, M.; Eissen, J.P.; Martin, H.; Koga, K.T. Simple mixing as the major control of the evolution of volcanic suites in the Ecuadorian Andes. *Contrib. Mineral. Petrol.* **2010**, *160*, 297–312. [CrossRef]
48. Skjerlie, K.P.; Patiño Douce, A.E. The fluid-absent partial melting of a zoisite-bearing quartz eclogite from 1· 0 to 3· 2 GPa; implications for melting in thickened continental crust and for subduction-zone processes. *J. Petrol.* **2002**, *43*, 291–314. [CrossRef]
49. Sisson, T.W.; Ratajeski, K.; Hankins, W.B.; Glazner, A.F. Voluminous granitic magmas from common basaltic sources. *Contrib. Mineral. Petrol.* **2005**, *148*, 635–661. [CrossRef]
50. Laurent, O.; Martin, H.; Moyen, J.F.; Doucelance, R. The diversity and evolution of late-Archean granitoids: Evidence for the onset of "modernstyle" plate tectonics between 3.0 and 2.5 Ga. *Lithos* **2014**, *205*, 208–235. [CrossRef]
51. Chappell, B.W. Aluminium saturation in I-and S-type granites and the characterization of fractionated haplogranites. *Lithos* **1999**, *46*, 535–551. [CrossRef]
52. Bonin, B. A-type granites and related rocks: Evolution of a concept, problems and prospects. *Lithos* **2007**, *97*, 1–29. [CrossRef]
53. White, A.J.R.; Chappell, B.W. Granitoid types and their distribution in the Lachlan Fold Belt, southeastern Australia. *Geol. Soc. Am. Mem.* **1983**, *159*, 21–34.
54. Kleemann, G.J.; Twist, D. The compositionally-zoned sheet like granite pluton of the Bushveld Complex: Evidence bearing on the nature of A-type magmatism. *J. Petrol.* **1989**, *30*, 1383–1414. [CrossRef]
55. Chappell, B.W.; White, A.J.R.; Hine, R. Granite provinces and basement terranes in the Lachlan Fold Belt, southeastern Australia. *Aust. J. Earth Sci.* **1988**, *35*, 505–521. [CrossRef]
56. Eby, G.N. Chemical subdivision of the A-type granitoids: Petrogenetic and tectonic implications. *Geology* **1992**, *20*, 641–644. [CrossRef]
57. Pearce, J.A.; Harris, N.B.; Tindle, A.G. Trace element discrimination diagrams for the tectonic interpretation of granitic rocks. *J. Petrol.* **1984**, *25*, 956–983. [CrossRef]
58. Maniar, D.D.; Piccolo, P.M. Tectonic Discrimination of granitoids. *Geol. Soc. Am. Bull.* **1989**, *101*, 635–643. [CrossRef]
59. Batchelor, R.A.; Bowden, P. Petrogenetic interpretation of granitoid rock series using multicationic parameters. *Chem. Geol.* **1985**, *48*, 43–55. [CrossRef]
60. Johannes, W.; Holtz, F. *Petrogenesis and Experimental Petrology of Granitic Rocks*; Springer Science & Business Media: Berlin/Heidelberg, Germany, 1996.
61. Jung, S.; Pfänder, J.A. Source composition and melting temperatures of orogenic granitoids: Constraints from CaO/Na_2O, Al_2O_3/TiO_2 and accessory mineral saturation thermometry. *Eur. J. Mineral.* **2007**, *19*, 859–870. [CrossRef]
62. Watson, E.B.; Harrison, T.M. Zircon saturation revisited: Temperature and composition effects in a variety of crustal magma types. *Earth Planet. Sci. Lett.* **1983**, *64*, 295–304. [CrossRef]
63. Boehnke, P.; Watson, E.B.; Trail, D.; Harrison, T.M.; Schmitt, A.K. Zircon saturation re-revisited. *Chem. Geol.* **2013**, *351*, 324–334. [CrossRef]
64. Miller, C.F.; McDowell, S.M.; Mapes, R.W. Hot and cold granites? Implications of zircon saturation temperatures and preservation of inheritance. *Geology* **2003**, *31*, 529–532. [CrossRef]
65. Condie, K.C.; Hunter, D.R. Trace element geochemistry of Archean granitic rocks from the Barberton region, South Africa. *Earth Planet. Sci. Lett.* **1976**, *29*, 389–400. [CrossRef]
66. Dall'Agnol, R.; de Oliveira, D.C. Oxidized, magnetite-series, rapakivi-type granites of Carajás, Brazil: Implications for classification and petrogenesis of A-type granites. *Lithos* **2007**, *93*, 215–233. [CrossRef]
67. Robinson, F.A.; Foden, J.D.; Collins, A.S.; Payne, J.L. Arabian Shield magmatic cycles and their relationship with Gondwana assembly: Insights from zircon U–Pb and Hf isotopes. *Earth Planet. Sci. Lett.* **2014**, *408*, 207–225. [CrossRef]
68. Stern, R.J.; Johnson, P.R.; Kroner, A.; Yibas, B. Neoproterozoic ophiolites of the Arabian-Nubian Shield. In *Precambrian Ophiolites and Related Rocks*; Kusky, T., Ed.; El-Sevier: Amsterdam, The Netherlands, 2004; Volume 13, pp. 95–128, Chapter 3.
69. Johnson, P.R.; Andresen, A.; Collins, A.S.; Fowler, A.R.; Fritz, H.; Ghebreab, W.; Kusky, T.; Stern, R. J. Late Cryogenian–Ediacaran history of the Arabian-Nubian Shield: A review of depositional, plutonic, structural, and tectonic events in the closing stages of the northern East African Orogen. *J. Afr. Earth Sci.* **2011**, *61*, 167–232. [CrossRef]

70. Stern, R.J.; Johnson, P. Continental lithosphere of the Arabian Plate: A geologic, petrologic, and geophysical synthesis. *Earth-Sci. Rev.* **2010**, *101*, 29–67. [CrossRef]
71. Stern, R.J. Neoproterozoic crustal growth: The solid Earth system during acritical episode of the Earth history. *Gondwana Res.* **2008**, *14*, 33–50. [CrossRef]
72. Greiling, R.O.; Abdeen, M.M.; Dardir, A.A.; El Akhal, H.; El Ramly, M.F.; El Din Kamal, G.M.; Osman, A.F.; Rashwan, A.A.; Rice, A.H.N.; Sadek, M.F. A structural synthesis of the Proterozoic Arabian–Nubian Shield in Egypt. *Geol. Rundschau* **1994**, *83*, 484–501. [CrossRef]
73. Genna, A.; Nehlig, P.; Le Goff, E.; Gguerrot, C.C.; Shanti, M. Proterozoic tectonism of the Arabian Shield. *Precambrian Res.* **2002**, *117*, 21–40. [CrossRef]
74. Farahat, E.S.; Mohamed, H.A.; Ahmed, A.F.; El Mahallawi, M.M. Origin of I- and 60. A-typegranitoids from the Eastern Desert of Egypt: Implica-tions for crustal growth in the northern Arabian-Nubian Shield. *J. African Earth Sci.* **2007**, *49*, 43–58. [CrossRef]
75. Farahat, E.S.; Zaki, R.; Hauzenberger, C.; Sami, M. The Neoproterozoic calc-alkaline peraluminous granitoids of the Deleihimmi pluton, central Eastern Desert, Egypt: Implications for transition from late- to post-collisional tectono-magmatic evolution in the northern Arabian–Nubian Shield. *Geol. J.* **2011**, *46*, 544–560. [CrossRef]